Remote Sensing of Environment 115 (2011) 1326–1340

Contents lists available at ScienceDirect

Remote Sensing of Environment

journal homepage: www.elsevier.com/locate/rse

Comparison of two temperature differencing methods to estimate daily evapotranspiration over a Mediterranean vineyard watershed from ASTER data

Mauricio Galleguillos [a], Frédéric Jacob [b,*], Laurent Prévot [a], Andrew French [c], Philippe Lagacherie [a]

[a] INRA/UMR LISAH, 34060, Montpellier, France
[b] IRD/UMR LISAH, 34060, Montpellier, France
[c] USDA/ALARC, Maricopa, AZ 85238, USA

ARTICLE INFO

Article history:
Received 3 August 2010
Received in revised form 15 January 2011
Accepted 16 January 2011
Available online 25 February 2011

Keywords:
Daily evapotranspiration
Vineyard
Mediterranean watershed
ASTER
S-SEBI
WDI
Validation
Model comparison
Spatial patterns

ABSTRACT

Daily evapo-transpiration (ET) was mapped at the regional extent over a Mediterranean vineyard watershed, by using ASTER imagery along with two temperature differencing methods: the Simplified Surface Energy Balance Index (S-SEBI) and the Water Deficit Index (WDI). Validation of remotely sensed estimates was conducted during almost two growth cycles (August 2007–October 2008) over seven sites that differed in soil properties, water status and canopy structure. S-SEBI and WDI were also intercompared at the watershed extent by considering ASTER imagery collected between 2002 and 2008. In order to alleviate the experimental efforts devoted to the validation exercise, ground truthing relied on in situ estimates from the HYDRUS-1D model that simulates water transfers within the vadose zone after calibration against measured soil moisture profiles. For two of the seven validation sites, the consistency of the HYDRUS-1D simulations was beforehand controlled against direct measurements with eddy covariance devices. Thus, it was shown the HYDRUS-1D simulations could be used as ground truthing.

Despite the use of simple differencing methods over a complex row-structured landscape, the obtained accuracies (0.8 mm.d^{-1} for S-SEBI and 1.1 mm.d^{-1} for WDI) were similar to those reported in the literature for simpler canopies, and fulfilled requirements for further applications in agronomy and hydrology. WDI performed worse than S-SEBI, in spite of more determinism within the derivation of evaporative extremes used for temperature differencing. This raised the question of compromising between process description and measurement availability. Analyzing validation results suggested that among the possible factors that could affect model performance (spatial variability, soil type and color, row orientation), the first-order influence was row orientation, a property that can be characterized from very high spatial resolution remote sensing data. Finally, intercomparing S-SEBI and WDI at the watershed extent showed estimates from both models agreed within 1 mm.d^{-1}, a difference similar to the model accuracies as estimated by the validation exercise. Then, time averaged maps suggested the existence of spatial patterns at the watershed extent, which may be ascribed to combined effects from soil type, soil depth and watertable level.

1. Introduction

Due to intimate links with micrometeorology and soil moisture, land surface evapotranspiration (ET) is a key variable for hydrology, agronomy and meteorology. Knowledge of daily ET is paramount in semiarid contexts, since daily ET corresponds up to 70% of the yearly water balance (Daneshkar, Arasteh, & Tajrishy, 2008; Moussa et al., 2007). Knowledge of daily ET is especially important for vineyards because grape yield and quality are critically dependent upon root zone moisture throughout the growth cycle. Vine crops in the Mediterranean region are often managed without irrigation. They are therefore subject to severe water stress, particularly before harvest (August–September) when evaporative demand is maximal while rainfall is insignificant. Water stress is necessary to regulate vegetative and fruit growth, canopy microclimate and fruit metabolism. However, excessive stress can cause severe damages in fruit development, thus affecting production and especially quality. Vineyard water status and daily ET should therefore be diagnosed at the appropriate growth stages. Additionally, water use in Mediterranean regions is characterized by increasing competition between the actors (including agriculture, industry and tourism), which can affect vineyards through watertable extraction. The competition may be further sharpened under the influence of global warming, where the Mediterranean region has been recognized as a Hot-Spot (Diffenbaugh et al., 2007; Giorgi, 2006). Vineyard water status and daily ET in Mediterranean regions should therefore be prognosticated under the influence of global change.

The estimation of vineyard ET has been investigated in several studies over the last two decades. The field scale has often been

* Corresponding author.
E-mail address: frederic.jacob@supagro.inra.fr (F. Jacob).

0034-4257/$ – see front matter © 2011 Elsevier Inc. All rights reserved.
doi:10.1016/j.rse.2011.01.013

considered, by implementing soil water balance models (Lebon et al., 2003; Pellegrino et al., 2006), by estimating latent heat flux (*LE*) from micrometeorological measurements (Heilman et al., 1994; Li et al., 2008; Li et al., 2009; Oliver & Sene, 1992; Ortega-Farias et al., 2007; Sene, 1994; Trambouze et al., 1998) or by estimating *LE* as the energy balance residual (Giordani et al., 1996; Spano et al., 2000). Meanwhile, the use of remote sensing to address larger scales was confined to the monitoring of vine physiological conditions, by using chlorophyll fluorescence indexes or changes in canopy reflectance (Flexas et al., 2000; Montero et al., 1999; Moya et al., 2004; Zarco-Tejada et al., 2005). On the other hand, remote sensing models devoted to ET estimation have been mostly applied over full canopies or sparse vegetation (Boegh et al., 2009; Courault et al., 2009; Hoedjes et al., 2008; Olioso et al., 2005; van der Kwast et al., 2009; Zwart & Bastiaanssen, 2007), with a desired accuracy of 0.8 $mm.d^{-1}$ at the daily timescale (Kalma et al., 2008; Seguin et al., 1999). Thus, very little information is available for vineyard ET, where row structures induce specific problems such as the influence of air turbulence within the canopy and inter-row on convective fluxes (Heilman et al., 1996), or the influence of shade effects on remote sensing data (Wassenaar et al., 2001; Zarco-Tejada et al., 2005).

Several methods, either empirical or deterministic, are candidate for mapping vineyard daily ET from remote sensing (Courault et al., 2005; Kalma et al., 2008). Among these candidates, the relevant choice for row structured vineyards is a two source modeling that discriminates soil and vegetation components (Norman et al., 1995; Sanchez et al., 2008) and even differentiates sunlit and shaded components (van der Tol et al., 2009; Verhoef et al., 2007). Nevertheless, a two source description requires information whose collection is not straightforward (e.g. net radiation, roughness lengths for momentum and heat, profiles within canopy for wind and leaf area index), and subsequent modeling errors may be large when considering row structured vineyards. An alternative possibility is using differencing methods that rely on spatial contrasts, where ET is characterized from differences in surface temperature rather than from absolute values (Gillies et al., 1997; Menenti & Choudhury, 1993; Moran et al., 1994; Roerink et al., 2000). This allows one to minimize errors on both data and parameterization, and to benefit from variabilities captured with high spatial resolution remote sensors (Gomez et al., 2005; Holifield et al., 2003; Mendez-Barroso et al., 2008; Moran et al., 1996; Sobrino et al., 2005; Sobrino et al., 2008), where the Advanced Spaceborne Thermal Emission and Reflection Radiometer (ASTER) sensor uniquely offers high quality spaceborne data of surface temperature (French et al., 2008; Jacob et al., 2004; Sabol et al., 2009; Sobrino, Jimenez-Munoz, et al., 2007).

The selection of differencing methods for the remote sensing of vineyard daily ET is driven by compromising between feasibility and accuracy. On the one hand, simple models are attractive since they are easy to implement and they usually perform as well as complex models (Kalma et al., 2008; Timmermans et al., 2007). Thus, contextual models allow one to avoid delicate calculations of biophysical variables, since the evaporative extremes used for the temperature differencing are beforehand estimated from the spatial variability captured within thermal imagery (Kalma et al., 2008). Good performances were reported by Galleguillos et al. (2011) when mapping vineyard daily ET with the Simplified Surface Energy Balance Index (S-SEBI) model proposed by Roerink et al. (2000). On the other hand, physically based models are more robust since the underlying physics gives portability. Thus, the Water Deficit Index (WDI) beforehand determines, by inverting surface energy balance, the evaporative extremes that are used for the temperature differencing, which involves ancillary information about aerodynamic and micro-meteorological conditions (Moran et al., 1994). Furthermore, S-SEBI and WDI differ in their characterization of the spatial variability: WDI makes use of the (surface–air temperature gradient, vegetation cover fraction) space (Gillies et al., 1997), whereas S-SEBI makes use of the (temperature, albedo) space (Bastiaanssen et al., 1998). This is of importance, since (i) albedo and vegetation cover fraction do not contain the same information, and (ii) temperature–albedo space may be more appropriate when land surfaces depict various vegetation types and phenological stages (Merlin et al., 2010).

The objective of this study is to compare the S-SEBI and WDI performances when estimating daily ET over a Mediterranean vineyard watershed, where the models are used along with ASTER imagery. For almost two growth cycles in 2007 and 2008, a comparison against ground truthing is conducted over seven validation sites distributed within the watershed, which allows both models to be tested for a range of conditions, including canopy structure, soil type and watertable level. In order to gain greater insight across a large suite of environmental conditions (Choi et al., 2009; French et al., 2005; Jacob et al., 2004; Timmermans et al., 2007), an intercomparison of model estimates is also conducted at the extent of the regional watershed (65 km^2), by considering ASTER imagery collected between 2002 and 2008. We first present the study site (Section 2.1), the ground based and remote sensing data (Section 2.2), the in situ and remotely sensed estimates of daily ET (Section 2.3 and Section 2.4), as well as the assessment and validation strategies (Section 2.5). We next report results when controlling the consistency of ground based estimates (Section 3.1), when validating S-SEBI and WDI retrievals against ground based estimates (Section 3.2), and when intercomparing S-SEBI and WDI at the watershed extent (Section 3.3). Outcomes are finally discussed and confronted against literature materials (Section 4).

2. Material and methods

2.1. Study site: the Peyne watershed

The Peyne watershed (43.49°N, 3.37°E, 80 m above sea level) is located in the Languedoc–Roussillon region, southern France. This 65 km^2 size watershed contains vine mono-cultures (70%) that are mostly rainfed (more than 95%). The remaining 30% include olive and wheat crops, native scrublands, forested areas, urban zones and water bodies. Annual rainfall ranges from 400 mm to 1300 mm, with a bimodal distribution in autumn and spring and a significant inter-annual variability (Trambouze & Voltz, 2001). Yearly Penman ET is close to 1100 mm. Vineyards are located over relatively flat terrain that depict 3% slopes in average (1.5° inclination), whereas 90% of these terrain have slopes lower than 8% (4.5° inclination).

The area holds a large suite of conditions for soil (with various parent materials) and watertable level that induce differences in water availability for vine plants. To capture this variability for validation purposes, seven sites corresponding to rainfed vineyards were selected (Table 1). They depicted similar trellis structures (2.5 m row spacing, 1 m maximum row width and 1.5 m averaged canopy height) apart from row orientation. Each of Site 1 to 5 and 7 corresponded to one field, with size ranging from 0.03 to 0.09 km^2. Site 6, with a 0.15 km^2 size, spread over nine contiguous fields including vineyards by 90% in surface area. It was split into north (6N) and south (6S) sub-sites for validation purposes.

2.2. Data

The validation exercise, which lasted between August 2007 and October 2008, was designed to alleviate experimental efforts for cost, device maintenance and data collection. Among the existing possibilities for in situ estimation of daily ET, we used the HYDRUS-1D model that simulates water transfers within the vadose zone after calibration against soil moisture profiles, provided meteorological forcing and watertable level are known. This alternate method was first assessed through a comparison against reference measurements

Table 1
Main characteristics of the validation sites within the Peyne watershed. The "Devices" column indicates (i) the number of locations within each site for collecting soil moisture profiles from Neutron Probe (NP) device, (ii) the collection of Eddy Covariance (EC) measurements when applicable, and (iii) the collection of net radiation (Rn) measurements when applicable. Each location of NP data was equipped for piezometric measurements. EC footprint over Site 6 encompassed both sub-sites 6N and 6S, whereas Rn footprint on Site 6 encompassed sub-site 6N only. Row orientation was characterized through row azimuth, where north is origin and positive values are clockwise. A soil was considered as shallow when the depth to parent material was less than 2.5 m. An absent watertable (respectively permanent watertable) means a piezometric level below 2.5 m depth (respectively above 2.5 m depth) throughout the year. A seasonal watertable means a piezometric level above 2.5 m depth during winter and spring.

Site number	Devices	Soil depth	Soil texture	Watertable conditions	Size (m^2)	Row azimuth (°)
1	1 NP	Shallow	Sandy, silty	Absent	32701	343
2	1 NP	Shallow	Clay, gravels	Seasonal	74966	42
3	2 NP	Shallow	Silty, sandy	Absent	29894	326
4	1 NP	Deep	Clay loam	Permanent	53851	24
5	2 NP	Deep	Clay	Seasonal	81052	35
6N	5 NP, EC, Rn	Deep	Clay loam	Seasonal	87493	85
6S	4 NP, EC	Shallow	Silty	Absent	58328	359
7	1 NP, EC	Deep	Clay	Absent	92312	318

from Eddy Covariance (EC) devices. EC devices were setup on two of the seven validation sites (Site 6 and 7).

The intercomparison of S-SEBI and WDI at the extent of the regional watershed required few ground based observations only (i.e. meteorological records). It was therefore possible to consider a larger temporal window than that selected for the validation exercise (August 2007–October 2008), and we included the whole set of ASTER imagery collected over the Peyne watershed from 2002.

We present hereafter the in situ measurements used to implement the ground truthing procedure, and next the ASTER remote sensing data to be used along with S-SEBI and WDI. Table 2 displays the spatial and temporal features of the dataset collected for (i) assessing the relevance of the HYDRUS-1D simulations through a comparison against EC measurements within two of the seven validation sites, (ii) validating the S-SEBI and WDI estimates of daily ET against HYDRUS-1D simulations within the seven validation sites and (iii) intercomparing the S-SEBI and WDI estimates of daily ET at the extent of the Peyne watershed.

2.2.1. Ground based data

EC devices were setup for continuous measurements of daily ET within two validation sites that differed in canopy structure, soil hydrodynamic properties and watertable dynamics: a permanent flux tower on Site 6, and a temporary flux station on Site 7 for three day windows centered on ASTER overpasses. Each flux station was equipped with a R.M. Young 81000 3D sonic anemometer and a fast hygrometer (Licor LI7500 for Site 6 and Campbell KH2O for Site 7) to measure wind speed components, air temperature and humidity. For Site 6 (respectively Site 7), the sensors were setup 5.7 m (respectively 1.5 m) above canopy and acquisition frequency was 10 Hz (respectively 20 Hz). EC footprint over Site 6 encompassed both sub-sites 6N and 6S.

Hourly values of air temperature, wind speed, relative humidity, solar irradiance and rainfall were continuously collected at Site 6 with a CIMEL ENERCO 400 station, by following meteorological standards apart from wind speed (measured at 2 m height rather than 10 m for agrometeorological purposes). Hourly net radiation was continuously measured over a representative vineyard within Site 6, by using a Campbell NR-lite device. Vine canopy within the NR-lite footprint ranged between 0% in winter (dormant vegetation with no leaves) and 66% in summer (active vegetation along with maximum vegetation cover fraction).

In order to infer daily ET from HYDRUS-1D simulations, each of the seven validation sites was monitored for soil moisture, watertable level and vegetation canopy structure. The data collection included the following items.

- Soil moisture profiles were sampled every 0.2 m down to 2.5 m with a Vectra 503-DR CPN Neutron Probe (NP) device, and completed for the top 0.15 m using a Soil Moisture Equipment TRASE 6050 Time Domain Reflectometry sensor. Within each site, the number of locations for collecting profiles (Table 1) varied according to site size and to soil heterogeneity derived from a pedological map. Profiles were collected around local solar noon, biweekly and after each significant (i.e. large or lengthy) rainfall.
- Soil horizons were characterized for depth and texture, by using in situ observations and expert knowledge. This was performed once at all sites, for each location of soil moisture profile.
- Watertable level was monitored down to 2.5 m, either continuously at Site 6 by using automated piezometric devices, or intermittently (i.e. with a two week frequency and after each significant rainfall, around local solar noon) at other sites by using manual piezometric devices. In accordance with continuous observations at Site 6, data collected on the other sites were linearly interpolated at the hourly timescale.
- Vegetation was monitored for canopy structure (height above soil for base and top of canopy, canopy width), over one (Site 1 to 5 and 7) or more (Site 6) fields. Following Trambouze (1996), these observations were performed in winter (dormant vegetation with no leaves) and in summer (period of maximum vegetation cover), and they were next linearly interpolated at the daily timescale. On average over the seven validation sites, canopy height was 1.5 m with a 0.1 m standard deviation (7% in relative) and canopy width was 1 m with a 0.1 m standard deviation (10% in relative). Row orientation and spacing were measured once.

Table 2
Spatial and temporal features of the dataset along with the corresponding investigations. The spatial features include the locations of ground based measurements when applicable and the spatial extents. The temporal features include the period of data acquisition for both ground based measurements and ASTER imageries.

	03/2002–07/2007	08/2007–10/2008
Site 6 and 7 Ground based data for • HYDRUS-1D simulations • EC measurements		Assessing the consistency of HYDRUS-1D simulated daily ET through comparison against EC measurements No ASTER imagery
Site 1 to 7 Ground based data for • HYDRUS-1D simulations • ASTER net radiation, WDI vertexes and ET_0.		Validating S-SEBI and WDI estimates of daily ET against the HYDRUS-1D simulations 11 ASTER imageries
Peyne watershed Ground based data (Site 6) for • ASTER net radiation, WDI vertexes and ET_0.	Intercomparing S-SEBI and WDI estimates of daily ET at the extent of the Peyne regional watershed 9 ASTER imageries	11 ASTER imageries

The ground based data above-presented were collected from August 2007 to October 2008, apart from meteorological data that were collected on Site 6 since 2002. Each instrument was manufacturer calibrated, apart from NP device that was calibrated to account for soil type and soil moisture. Calibration was performed against gravimetric soil moisture data at each measurement depth (soil density was estimated using a Campbell DR 501 gamma probe). The calibration residual error was 0.04 $m^3.m^{-3}$ (15% relative error).

2.2.2. Remote sensing data

We used ASTER official products for surface reflectance, waveband emissivity and radiometric temperature (Abrams, 2000). Their accuracies were 5%, 0.01 and 1.5 K respectively (Jacob et al., 2008; Sabol et al., 2009; Sobrino, Jimenez-Munoz, et al., 2007; Thome et al., 1998). These products resulted from 20 scenes sun-synchronously collected under clear sky conditions around 11:00 UTC with a close-nadir viewing. Among these 20 scenes, 11 could be used for validation exercises thanks to simultaneous ground based measurements: three in 2007 (14 Aug, 15 Sep, and 2 Nov) and eight in 2008 (22 Jun, 8 Jul, 15 Jul, 24 Jul, 31 Jul, 1 Sep, 26 Sep, and 3 Oct). Nine archive scenes were also considered for model comparison at the watershed extent: two in 2002 (13 Jun, and 29 Jun); one in 2003 (8 Feb); three in 2005 (20 May, 27 May, and 15 Aug); one in 2006 (10 Jul) and two in 2007 (10 May, and 13 Jul). Reflectances at 15 m (visible and near infrared) or 30 m (shortwave infrared) were averaged at the 90 m resolution of the thermal infrared products (emissivity and radiometric temperature). Images were then geolocated against a 0.5 m spatial resolution aerial orthophotograph collected in summer 2007.

2.3. In situ estimation of daily ET

2.3.1. Direct estimation from EC measurements

For Site 6 and 7, sensible and latent heat fluxes were calculated over hourly intervals from the EC measurements, by applying the whole set of instrumental corrections and the double rotation correction proposed by the ECPACK 2.5.20 library (Dijk et al., 2004). Fluxes were calculated along with tolerance intervals, where the latter were about 20% and 12% in relative for Site 6 and 7, respectively. When checking energy balance closure as an indicator of EC data quality, convective fluxes and available energy agreed within 80% in relative. Daily ET was finally calculated as the sum of hourly ET between sunrise and sunset.

2.3.2. Indirect estimation from HYDRUS-1D model simulations

For the seven validation sites, ground truthing of daily ET was obtained from simulations of HYDRUS-1D (Simunek et al., 2008) which is a physically-based model that simulates water flow in the vadose zone from Richards equation (Richards, 1931):

$$\frac{\partial \theta}{\partial t} = \frac{\partial}{\partial z}\left[K\left(\frac{\partial h}{\partial z} + cos(\beta)\right)\right] - S(h) \quad (1)$$

where θ is volumetric water content, t is time, z is vertical ascending coordinate, K is unsaturated hydraulic conductivity, β is the angle between the water flow and the vertical axis ($\beta = 0°$ for ascending flow). The sink term $S(h)$ represents water uptake by roots as a function of pressure head h, and corresponds to the volume of extracted water per soil volume unit and per time unit. We present here the model implementation and the derivation of daily ET from model simulations of actual plant transpiration and soil evaporation.

Meteorological forcing included rainfall and reference evapotranspiration ET_0. Rainfall was measured at the meteorological station (Section 2.2.1). Following Riou et al. (1994), ET_0 was estimated from the data collected at the meteorological station, by using the Penman formulation under standard conditions that can be found in Valiantzas (2006). ET_0 was then split into reference transpiration T_0 and reference evaporation E_0, by using the Riou's model designed for vineyards (Bsaibes, 2007; Riou et al., 1994; Trambouze & Voltz, 2001). First, T_0 was calculated as a fraction of ET_0, by assuming this fraction is almost equal to the ratio of solar irradiance absorbed by vine leaves R_v (geometrically derived from solar position and canopy structure) to that absorbed by the whole vineyard $(1-a_v)R_g$:

$$T_0 = ET_0 \frac{R_v}{(1-a_v)R_g} \quad (2)$$

where R_g is solar irradiance. Vineyard albedo a_v was set to 0.2 (Bsaibes, 2007). This was done for the seven validation sites whose trellis structures were similar apart from row orientation (Section 2.1). Second, E_0 was determined as the residual of the ET_0 splitting into T_0 and E_0 : $E_0 = ET_0 - T_0$. Next, vine maximum transpiration T_m was set to reference transpiration T_0, which was within the confidence interval reported by Trambouze and Voltz (2001) who suggested a 10% larger value.

The soil was split into a limited number of horizons (between two and four including topsoil, in accordance with in situ observations and expert knowledge, Section 2.2.1), and discretized into 251 layers between 0 and 2.5 m depth. Root density was distributed according to in situ observations and outcomes from previous studies (Bsaibes, 2007; Trambouze & Voltz, 2001). The resulting averaged profile considered 75% of roots between 0.25 and 1.25 m, with a 2.2 m maximum depth. The sink term $S(h)$ was calculated as the product of two functions. The first function represented the layer maximum transpiration, expressed as the product of T_0 and root relative density (i.e. root density for the layer divided by the cumulated density over the root profile). The second function represented the modulation of maximum transpiration according to soil moisture. It was expressed by using the Feddes functions that depend on soil water potential (Feddes et al., 1978), where threshold pressures were set at −0.1 mbar and −1.5 mbar by following observations from Trambouze and Voltz (2001) for vineyards. Lower boundary conditions were set to free outflow when piezometric data indicated watertable absence, and to fixed pressure head at the watertable level otherwise.

For each soil horizon, unsaturated hydraulic conductivity and retention curves were characterized using the van Genuchten functions that depend on (i) residual θ_r and saturated θ_s soil moisture, (ii) saturated hydraulic conductivity K_s, (iii) bubbling pressure α and (iv) pore-size distribution index n (van Genuchten, 1980). For each soil horizon, θ_r and θ_s were set to maximum and minimum soil moisture values throughout time series of NP measurements (biweekly observations between August 2007 and October 2008, Section 2.2.1). For topsoil (first horizon), the three other inputs of van Genuchten functions (K_s, α and n) were estimated by following previous studies over the Peyne watershed (Bsaibes, 2007; Trambouze & Voltz, 2001). For deeper horizons, they were determined by using the HYDRUS-1D inverse mode, where the cost function to be minimized was the quadratic difference between measured and simulated soil moisture profiles over the simulation period. Initial guesses for the three parameters to be estimated were derived from in situ observations and expert knowledge (Section 2.2.1), from previous studies for similar soils (Bsaibes, 2007; Trambouze & Voltz, 2001), or from the HYDRUS-1D ROSETTA module.

Actual evapotranspiration was calculated as the sum of soil evaporation and plant transpiration. First, plant transpiration was calculated as the sum of root water uptake $S(h)$ over all layers. Second, soil evaporation was simulated using the Neuman's conditionality, where evaporation is driven by E_0, surface pressure head and soil moisture (Neuman et al., 1974). The threshold values were set to −10 m (respectively +0.01 m) for the minimum (respectively maximum) soil potential pressure that corresponds to conditions of complete dryness (respectively runoff initiation).

For each location where soil moisture profiles were collected with NP measurements (Table 1), HYDRUS-1D was calibrated against the resulting time series that spanned the [August 2007–October 2008] period. Calibration relied on noon values, since NP data acquisition periods were centered on noon (Section 2.2.1). Hourly simulations allowed one to account for changes in sunlit and shadow within vineyard rows, and resulting ET was aggregated at the daily timescale.

2.4. Remote sensing estimation of daily ET

The data to be used as inputs for S-SEBI and WDI are listed in Table 3. The obtaining of these inputs and the resulting implementation of both models are presented in the current section.

2.4.1. Meteorological and biophysical inputs for S-SEBI and WDI models

Values of meteorological variables at the time of ASTER overpass were obtained by interpolating the hourly data collected at the meteorological station (Section 2.2.1). Air temperature and solar irradiance were interpolated using the formulations proposed by de Wit et al. (1978) and Jackson et al. (1983), respectively. Air humidity, wind speed and atmospheric pressure were linearly interpolated, since they did not depict any specific temporal behavior at the day or half-day timescales.

The Soil Adjusted Vegetation Index (SAVI) proposed by Huete (1988) was considered for characterizing vegetation cover fraction from ASTER images, where SAVI is defined as (ρ_{nir} are ρ_{red} are surface reflectances over near infrared and red wavebands):

$$SAVI = (1 + L)\frac{\rho_{nir} - \rho_{red}}{\rho_{nir} + \rho_{red} + L} \quad (3)$$

The choice of this index was motivated by its ability to account for soil effects, which was appropriated for studying row structured vineyards. The coefficient L (soil adjusted constant) was set to 1/2 by following Huete et al. (1992) for a large variety of vegetation canopies, since no value was proposed for vineyards.

Net radiation R_n was derived from ASTER imagery by using the standard formulation (Chehbouni et al., 2008; Courault et al., 2003; Er-Raki et al., 2007; Jacob et al., 2002), where σ is the Stefan Boltzmann constant:

$$R_n = (1 - a_s)R_g + \varepsilon_s\left(R_a - \sigma T_s^4\right) \quad (4)$$

This required beforehand estimating the involved components.

- Albedo a_s was computed as a linear combination of ASTER waveband reflectances. Due to deficient shortwave infrared channels in 2008, we used the generic two channel (red and near infrared) formulation proposed by Weiss et al. (1999), where the latter was beforehand linearly corrected against the ASTER seven channel formulation (visible–near infrared–shortwave infrared) proposed by Liang (2001). The linear correction was calibrated over the 2007 ASTER dataset, with a relative unsystematic error of 6%, and was applied to the 2007–2008 ASTER dataset. Accuracy on a_s was calculated as the quadratic combination of (i) the accuracy of the ASTER seven channel formulation and (ii) the unsystematic error on the linear correction of the generic two channel formulation. This yielded an accuracy of about 0.20 in absolute (10% in relative).
- Broadband emissivity ε_s was computed as a linear combination of ASTER waveband emissivities, by following Ogawa et al. (2003).
- Atmospheric irradiance R_a was estimated from measurements of air temperature and vapor pressure collected at the meteorological station (Section 2.2.1), by using the formulation proposed by Brutsaert (1975) for clear-sky conditions.
- Solar irradiance R_g was derived from measurements collected at the meteorological station (Section 2.2.1).
- Surface temperature T_s was provided by ASTER official products (Section 2.2.2).

Finally, soil heat flux G_0 was derived from ASTER imagery using the formulation proposed by Clothier (1986), where G_0 is expressed as a fraction of net radiation R_n:

$$G_0 = R_n\left(0.295 - 0.01331\frac{\rho_{nir}}{\rho_{red}}\right) \quad (5)$$

This formulation was chosen since it was recommended by Moran et al. (1994) when implementing WDI along with optical remote sensing imagery.

2.4.2. S-SEBI estimates of daily ET

Below is a model overview, see Roerink et al. (2000), Gomez et al. (2005), Verstraeten et al. (2005), and Sobrino et al. (2005) for detailed descriptions. Deriving daily ET, ET_d, from S-SEBI along with optical imagery, where the latter captures contrasts driven by evaporation processes, is twofold. Evaporative fraction Λ, the ratio of latent heat flux to available energy, is firstly computed from the differences between surface temperature T_s and extreme temperatures (T_{max} and T_{min} for maximum and minimum temperature, respectively) within a given albedo class, where the extreme temperatures are those captured within ASTER thermal imagery. Second, assuming the instantaneous Λ at satellite overpass is equal to the daily Λ, and neglecting daily soil heat flux, ET_d is derived from Λ by extrapolating, at the daily timescale, instantaneous net radiation at satellite overpass R_{ni}. This is performed using the ratio $Cd_i = R_{nd}/R_{ni}$ where R_{nd} is daily net radiation. Overall, the twofold procedure yields (L is latent heat of vaporization):

$$ET_d = \Lambda\frac{R_{nd}}{L} = \frac{T_{max} - T_s}{T_{max} - T_{min}}\frac{Cd_i R_{ni}}{L} \quad (6)$$

S-SEBI was implemented along with ASTER imagery as following (Fig. 1). The temperature–albedo space was characterized by calculating, for each 10^{-3} width albedo class, mean albedo and

Table 3
Listing of the model inputs for WDI and S-SEBI, when differentiating inputs derived from (i) ground based measurements only, (ii) remotely sensed measurements only, (iii) both ground based and remotely sensed measurements and (iv) other sources of information (e.g. bibliographic).

		Model	
		S-SEBI	WDI
Inputs	Derived from ground based measurements only	Ratio of daily to instantaneous values of net radiation (2)	Solar irradiance (1) Air temperature (1) Air humidity (1) Atmospheric pressure (1) Wind speed (1)
	Derived from remotely sensed measurements only	Surface Temperature Surface albedo	Surface Temperature SAVI
	Derived from both ground based and remotely sensed measurements	Instantaneous net radiation	Instantaneous net radiation (1) Instantaneous soil heat flux (1)
	Derived from bibliography (aerodynamic properties and vegetation parameters)		Canopy resistances (1) Roughness length (1) kB^{-1} parameter (1)

(1) For calculations of WDI vertexes and/or ET_0 (Section 2.4.3).
(2) Instantaneous values at ASTER overpass (11:00 UTC).

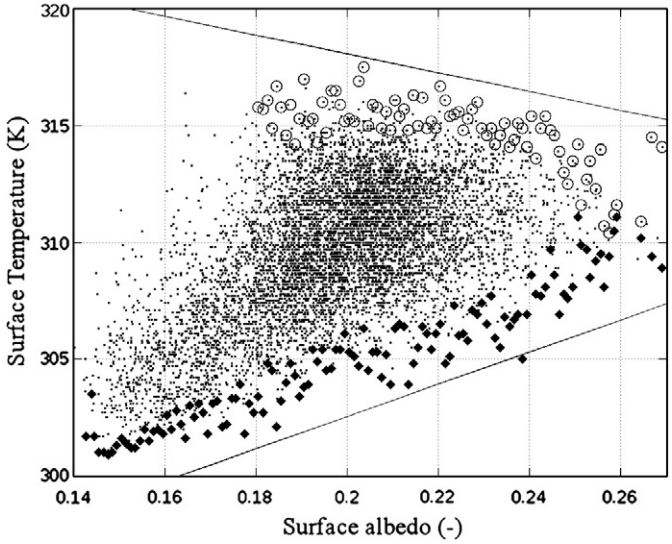

Fig. 1. Typical example of the scatterplots we obtained for the surface temperature (y-ordinate) versus albedo (x-abscissa) diagram used to compute evaporative fraction with S-SEBI. Full diamonds correspond to the (temperature–albedo) pairs for minimum temperature values of each albedo class, to be used for computing the lower limit through linear regression. Empty circles correspond to the (temperature–albedo) pairs for maximum temperature values of each albedo class, to be used for computing the upper limit through linear regression. Such a scatterplot was obtained for each of the 20 ASTER scenes we considered.

extreme temperatures. Next, T_{max} upper limit (respectively T_{min} lower limit) was determined from the linear regression between mean albedo and maximum (respectively minimum) temperature of each albedo class. As proposed by Roerink et al. (2000), T_{max} upper limit was computed by excluding albedoes below the threshold value that discriminates evaporative and radiative regimes, where the threshold albedo corresponds to the maximum temperature of the concave temperature–albedo relationship (Bastiaanssen et al., 1998). To reduce noise influence, T_{min} lower limit was computed by including all albedoes (Verstraeten et al., 2005), rather than excluding classes above the threshold value (Roerink et al., 2000). To include all (temperature, albedo) pairs within the outer limits, an offset was added to T_{max} (respectively subtracted to T_{min}) regression line, where the offset equaled the standard deviation of maximum (respectively minimum) temperature over the albedo classes.

Following Gomez et al. (2005), the Cd_i coefficient was calibrated on a daily basis using ground based measurements of net radiation collected within Site 6 (Section 2.2.1). Therefore, the calibrated coefficient depended on satellite overpass time, and was assumed to be uniform within the Peyne watershed.

Applying S-SEBI over the Peyne watershed implicitly assumed the latter simultaneously held dry and wet areas at ASTER overpass times. This was consistent with the presence of bare soils, forested areas, rivers and water bodies. In order to preserve this variability, the whole watershed was considered within the ASTER imagery, without removing any part. Thus, estimating evaporative fraction from temperature differencing (Eq. (6)) implicitly assumed micro-meteorological and aerodynamic conditions were similar for all vegetation canopies within the watershed. Although this was far from reality, because of differences in roughness lengths, wind speed and Monin–Obukhov length, the resulting errors was expected to be low. Indeed, previous studies showed S-SEBI performed well when applied over various agrosystems that included patchworks of vegetation canopies (Boronina & Ramillien, 2008; Gomez et al., 2005; Roerink et al., 2000; Sobrino, Gomez, et al., 2007; Sobrino et al., 2005; Verstraeten et al., 2005).

2.4.3. WDI estimates of daily ET

Water Deficit Index (WDI) is a physically based index devoted to characterizing land surface water status (Moran et al., 1994). It is defined as the complementary to unity with the ratio of actual ET, ET_a, to maximum ET, ET_m. Similarly to S-SEBI, deriving daily ET from WDI along with optical remote sensing imagery is twofold. By assuming air temperature T_a is homogeneous within the study area, WDI is firstly computed from the differences between surface temperature T_{sB} and extreme temperatures (maximum T_{sC} and minimum T_{sA}) that correspond to the same vegetation cover fraction (see Fig. 2 for the setting of T_{sA}, T_{sB}, T_{sC}):

$$WDI = 1 - \frac{ET_a}{ET_m} = \frac{(T_s - T_a)_B - (T_s - T_a)_A}{(T_s - T_a)_C - (T_s - T_a)_A} = \frac{T_{sB} - T_{sA}}{T_{sC} - T_{sA}} \quad (7)$$

where the extreme temperatures T_{sC} and T_{sA} are determined from energy balance calculation. Once WDI is calculated, a second step consists of extrapolating values of instantaneous ET at the daily timescale. Assuming WDI is constant during daytime, similarly to Λ (Section 2.4.2), daily ET, ET_d, is computed by using an estimate of maximum evapotranspiration ET_m at the daily timescale ET_{md}:

$$ET_d = (1 - WDI) ET_{md} \quad (8)$$

The trapezoid displayed in Fig. 2 characterizes the possible extremes (in that sense they may not occur) in terms of vegetation cover fraction and water status. Segment 1–3 represents wet edge with well watered situations (WDI = 0) from bare soils to full canopies. Segment 2–4 represents dry edge with complete absence of water (WDI = 1) from bare soils to full canopies. Segment 1–2 (respectively 3–4) represents full canopies (respectively bare soils) from wet to dry conditions.

Whereas S-SEBI determines extreme temperatures from minimum and maximum values captured within thermal imagery (Section 2.4.2),

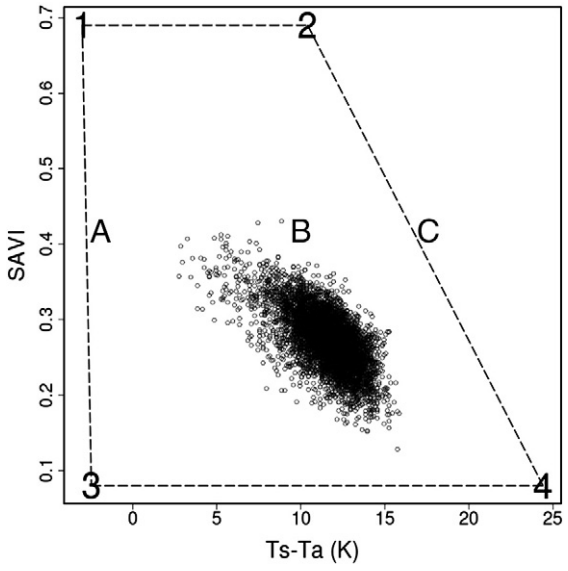

Fig. 2. Typical example of the scatterplots we obtained for the SAVI (y-ordinate) versus $T_s - T_a$ (x-abscissa) diagram used to compute WDI, where SAVI is used for characterizing vegetation cover fraction, and $T_s - T_a$ is surface–air temperature gradient. Numbers are vertices that allow one to determine possible extremes (in dotted lines). Segment 1–2 (respectively 3–4) corresponds to full canopies (respectively bare soils). Segment 1–3 (respectively 2–4) corresponds to wet edge with maximum evapotranspiration (respectively dry edge with negligible evapotranspiration). A, B and C are possible water status for a vineyard plot with a given vegetation cover fraction, where A is for fully wet condition, C is for complete dry condition and B is an intermediate situation that represent the pixel status. Such a scatterplot was obtained for each of the 20 ASTER scenes we considered.

WDI determines these extrema from energy balance calculation, provided net radiation, soil heat flux, meteorological and aerodynamic conditions are known. This determination relies on estimating the four vertices that delineate the trapezoid in Fig. 2, which consists of inverting the sensible heat flux formulation:

$$(T_s - T_a) = r_a\left(\frac{R_n - G_0}{C_p}\right)\left(\frac{\gamma(1 + r_c / r_a) - VPD}{\Delta + \gamma(1 + r_c / r_a)}\right) \quad (9)$$

where C_p is air isobaric specific heat that depends on T_a; γ is psychrometric constant that depends on T_a and atmospheric pressure P_a; Δ is the slope of the saturated vapor pressure–temperature relation that depends on T_a; VPD is air vapor pressure deficit that depends on T_a and air humidity e_a; R_n is net radiation; G_0 is soil heat flux; r_c is canopy resistance to vapor transport and r_a is aerodynamic resistance derived from the reference formulation of Thom (1975):

$$r_a = \frac{1}{k^2 u}\left[ln\left(\frac{z_r - d}{z_{0m}}\right) - \psi_m\left(\frac{z-d}{L_{MO}}\right)\right]\left[ln\left(\frac{z_r - d}{z_{0h}}\right) - \psi_h\left(\frac{z-d}{L_{MO}}\right)\right] \quad (10)$$

where k is Von Kármán constant, u is wind speed, z_r is reference height, d is displacement height, z_{0m} and z_{0h} are roughness lengths for momentum and heat respectively, ψ_m and ψ_h are stability correction functions for momentum and heat respectively, and L_{MO} is Monin–Obukhov length defined as :

$$L_{MO} = -\frac{\rho_a C_p u_*^3 T_a}{kgH} \quad (11)$$

where ρ_a is air density, u_* is friction velocity, g is gravity acceleration and H is sensible heat flux.

When implementing WDI along with ASTER imagery, the first step consisted of estimating maximum and minimum values for vegetation cover fraction, where the latter was characterized through SAVI (Section 2.4.1). Since no SAVI values were found in the literature for full canopies and bare soils within vineyards, we used the maximum and minimum values observed within the watershed and throughout the experiment that spanned two growth cycles.

The second step for implementing WDI along with ASTER imagery consisted of estimating the variables involved in the calculations of the four vertices (Fig. 2).

- C_p, γ, Δ and VPD were derived from measurements of air temperature T_a, air humidity e_a and atmospheric pressure P_a at the meteorological station (Section 2.2.1). Wind speed u was also derived from measurements at the meteorological station (Section 2.2.1).
- Determining net radiation R_n and soil heat flux G_0 for each of the four vertices was not straightforward. Indeed, these four extremes were not observed within the watershed, as illustrated by Fig. 2 where there is no data point near the vertices. We therefore considered the closest data points, by averaging R_n and G_0 values over pixels that corresponded to pairs of extremes values for SAVI and $T_s - T_a$ (i.e. $(SAVI)^{max}$ and $(T_s - T_a)^{max}$, $(SAVI)^{max}$ and $(T_s - T_a)^{min}$, $(SAVI)^{min}$ and $(T_s - T_a)^{min}$, $(SAVI)^{min}$ and $(T_s - T_a)^{max}$). These four pairs were derived from quantiles of SAVI and $T_s - T_a$.
- Canopy resistance r_c was determined for each vertex according to vegetation cover and water status. Vertex 1 corresponds to full-covering and well-watered vegetation, which yields $r_c = r_{cp}$ where r_{cp} is canopy resistance at maximum evapotranspiration. By following Ortega-Farias et al. (2007), r_{cp} over vineyards was set to 25 $s.m^{-1}$, although Sene (1994) suggested this value can range between 10 and 100 $s.m^{-1}$. Vertex 2 corresponds to full-covering vegetation without any water supply (ET is negligible), which induces $r_c = r_{cx}$ where r_{cx} is canopy resistance associated to nearly complete stomatal closure. By following Giordani et al. (1996), r_{cx} over vineyards was set to 2000 $s.m^{-1}$. Vertex 3 corresponds to a saturated bare soil with a negligible canopy resistance: $r_c = 0$ $s.m^{-1}$. Vertex 4 corresponds to a dry bare soil with an infinite canopy resistance equivalent to complete stomatal closure: $r_c = \infty$.
- Aerodynamic resistance r_a was also estimated for each of the four vertices. First, roughness length for momentum and displacement height were set to 3/100 and 2/3 of canopy height, respectively, by following Sene (1994) and Ortega-Farias et al. (2007). Second, the ratio z_{om}/z_{oh} was set to 100, as recommended by Giordani et al. (1996) for vineyards. The kB^{-1} factor was then close to five, which was lower than the value of eight obtained by Verhoef et al. (1996) for a vineyard site. Third, Monin–Obukhov length was estimated by discriminating well watered situations for which $L_{MO} = \infty$, and dry situations for which $H = Rn - G$ in Eq. (11). For dry situations, friction velocity u_* was derived from the EC measurements collected within Site 6 (Section 2.2.1).

Finally, maximum evapotranspiration at the daily timescale ET_{md} was set to reference evapotranspiration, by following outcomes from Williams and Ayars (2005) who reported values of grapevine crop coefficient close to one during the period of maximum vegetation cover. Reference evapotranspiration was derived from measurements at the meteorological station by using the Penman formulation (Section 2.3.2).

Conversely to S-SEBI, which has been widely used by including all vegetation canopies within the study area, Moran et al. (1994) recommended using WDI on a vegetation biome basis, where further studies acted accordingly (Holifield et al., 2003; Li & Lyons, 1999; Luquet et al., 2003; Vidal & Devaux-Ros, 1995; Wang & Takahashi, 1999). Therefore, assumption about aerodynamic resistance (i.e. r_a was identical for all vegetation canopies) was not as sharp as compared to S-SEBI, since it was restricted to a unique vegetation biome that might depict lower variabilities in terms of aerodynamic and meteorological conditions. For WDI implementation, vineyards within ASTER imagery were therefore selected by using a mask derived from cadastral maps and aerial orthophotographs.

2.5. Assessment strategy

The different steps of the assessment strategy, along with the involved ground based and remote sensing data, are listed in Table 2.

We firstly controlled the consistency of HYDRUS-1D simulations, by (i) quantifying calibration residual error (i.e. the differences between measured and simulated soil moisture profiles) over the seven validation sites within the Peyne watershed and (ii) comparing simulated daily ET against direct EC measurements over two of the seven validation sites (Site 6 and 7). We secondly validated S-SEBI and WDI estimates of daily ET against ground truthing (i.e. HYDRUS-1D simulations) over the seven validation sites. We thirdly compared S-SEBI and WDI estimates of daily ET at the extent of the whole watershed.

When comparing HYDRUS-1D simulated daily ET against EC estimates over Site 6, we averaged the nine HYDRUS-1D simulations that corresponded to the nine locations of NP measurements within the footprint of EC measurements (Table 1, Section 2.2.1 and Section 2.3.2). For Site 7, one HYDRUS-1D simulation only was involved, corresponding to one location of NP measurements within the footprint of EC measurements.

When validating ASTER/S-SEBI and ASTER/WDI estimates against HYDRUS-1D simulations of daily ET, we differentiated years and sites in relation to soil type, watertable conditions and canopy structure. For comparison over sites with two locations of NP measurements (Site 3 and 5), we averaged the two corresponding HYDRUS-1D simulations. For comparison over Site 6, HYDRUS-1D simulations were averaged for each sub-site 6N and 6S (Table 1, Section 2.2.1 and Section 2.3.2). From an ASTER viewpoint, we extracted each pixel

matching a site or sub-site. Finally, S-SEBI and WDI were inter-compared over vineyards only, since WDI did not provide any estimate due to the masking of other biomes.

From a growth cycle perspective, investigations were conducted by considering two situations: the whole dataset on the one hand, and the period of maximum vegetation cover on the other hand. Motivations for this were the following. First, the period of maximum vegetation cover is the most critical for vine quality. Second, the canopy conditions for the various sites within the watershed were more similar during this period. Third, most ASTER observations (75%) were collected during this period.

3. Results

3.1. Assessing the consistency of the HYDRUS-1D simulations

When averaged over all dates and locations of NP measurements, Root Mean Square Error (RMSE) between measured and simulated soil moisture decreased with depth, between 0.05 and 0.03 $m^3.m^{-3}$, with largest values (0.06 $m^3.m^{-3}$) around 1 m depth. These RMSE values corresponded to a range of relative RMSE (RRMSE) between 30 and 10%, where RRMSE was computed as the ratio of RMSE to reference mean value. When averaged over each profile, the RMSE between measurements and simulations varied from one date and one location to another, between 0 and 0.15 $m^3.m^{-3}$ (0% and 60% in relative). Lowest and largest RMSE values were observed within Site 4 and Site 1, respectively, but no evident link could be underlined with watertable conditions or soil type. For a given location, RMSE between measurements and simulations decreased with simulation time. When focusing on soil water storage at noon obtained by integrating moisture profile, RRMSE between simulations and measurements was around 10%.

RMSE between HYDRUS-1D estimates and EC measurements of daily ET was 0.4 $mm.d^{-1}$ (18% in relative) for Site 7, where water stress resulted from a deep watertable and a clay soil. For Site 6, with an intermediate water status related to a shallow watertable and silty/clay loam soils, RMSE was 0.6 $mm.d^{-1}$ (33% in relative). Merging statistics of both sites yielded an RMSE of 0.55 $mm.d^{-1}$ (32% in relative). Over the two sites, HYDRUS-1D simulations overestimated EC estimates for large ET values after significant rainfalls. Absolute RMSE was stable along the simulations, resulting in larger relative RMSE between August and December 2007 when ET was low, as compared to the [January–October] 2008 period. Similar results to those abovementioned were obtained with a dataset restricted to the period of maximum vegetation cover (Fig. 3a) or to ASTER overpass days (Fig. 3b), with RMSE of 0.6 $mm.d^{-1}$ (29% in relative) and 0.5 $mm.d^{-1}$ (22% in relative), respectively.

When focusing on HYDRUS-1D simulations of daily ET throughout the experimental period, an important temporal dynamics was observed for all sites, including seasonal variations, with values ranging from 0 to 6.5 $mm.d^{-1}$. An example is displayed in Fig. 4, for two contrasted sites in terms of pedology and watertable dynamics (Table 1). Site 1 corresponded to a shallow soil, with a sandy–silty texture, where absence of watertable induced restrictive water conditions for vine plants. Site 4 corresponded to a deep soil with a silty clay texture, where permanent watertable provided a continuous water supply for vine plants. As expected, the evapotranspiration rate was more important within Site 4 (averaged daily ET of 2.9 $mm.d^{-1}$) than within Site 1 (averaged daily ET of 2.1 $mm.d^{-1}$), whereas the temporal variability was lower for Site 4 (standard deviation of 1.1 $mm.d^{-1}$) than Site 1 (standard deviation of 1.5 $mm.d^{-1}$). An analysis at a finer timescale underlined specific periods with opposite trends. Over the [August–October] period, evapotranspiration was lower for Site 1 (daily ET values between 0 and 2 $mm.d^{-1}$) than Site 4 (daily ET values between 2 and 4 $mm.d^{-1}$), as expected. On the other hand, evapotranspiration was larger for Site 1 (daily ET values between 4 and 6 $mm.d^{-1}$) than Site 4 (daily ET values between 2 and 4 $mm.d^{-1}$) over the [May–July] period.

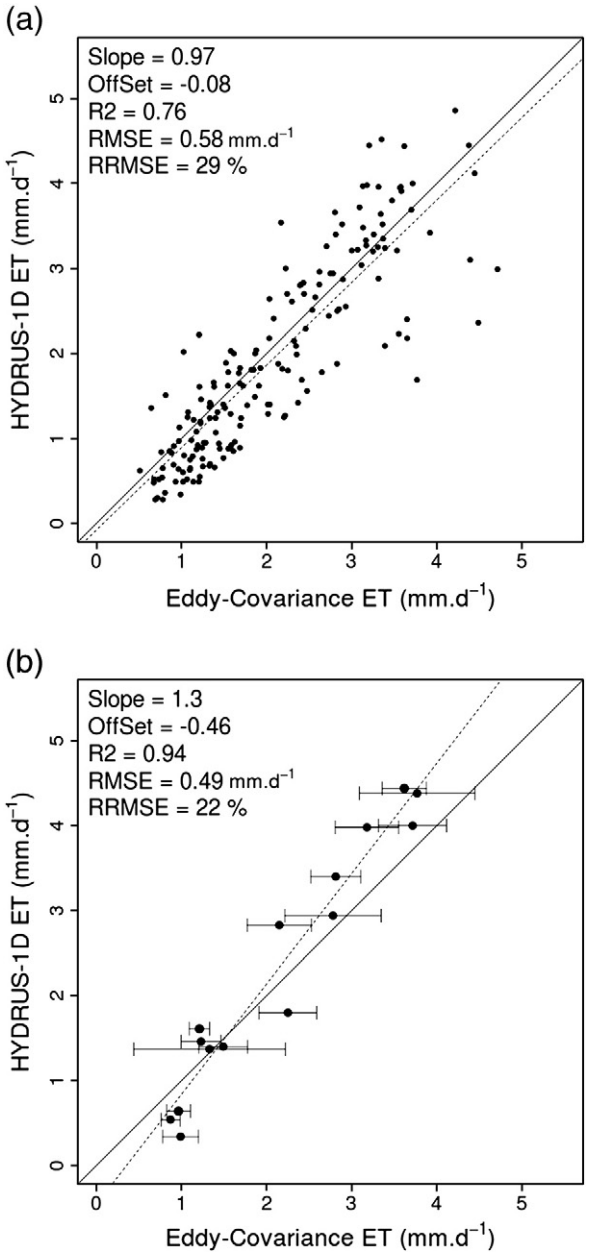

Fig. 3. Comparison of ET HYDRUS-1D estimates against EC measurements for Sites 6 and 7 when selecting (a) the period of maximum vegetation cover (1 Aug to 15 Oct 2007 and 1 Jul to 15 Oct 2008) and (b) ASTER overpasses only (error bars indicate the tolerance intervals provided by the ECPACK 2.5.20 library along with ET calculations from EC data). R2 is determination coefficient, Slope and Offset results from linear regression (dotted line) between x (reference estimates from EC measurements) and y (estimates from HYDRUS-1D simulations) axis data. RMSE is Root Mean Square Error. RRMSE is Relative Root Mean Square Error calculated as the ratio of RMSE to reference mean value. Continuous line is the 1:1 line.

3.2. Validating remotely sensed estimates

A first step focused on net radiation which is a key variable in S-SEBI and WDI calculations (Section 2.4.2 and 2.4.3). Validation of ASTER estimates against in situ measurements collected within Site 6 (Section 2.2.1) provided a RMSE of 45 $W.m^{-2}$. A second step aimed to quantify standard deviation of daily ET within 3×3 pixel windows centered on each of the seven validation sites, which provided an overall value of 0.4 $mm.d^{-1}$.

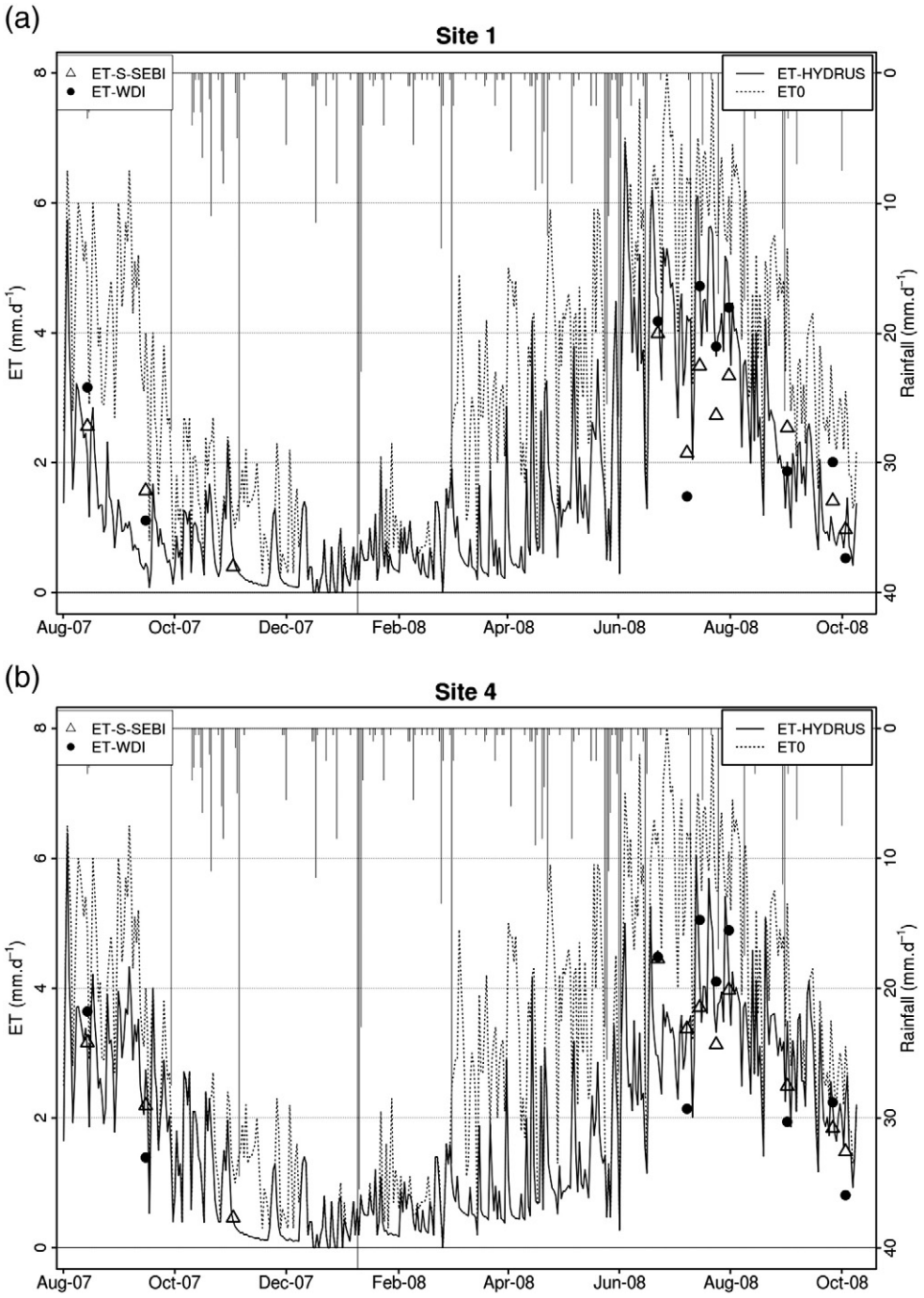

Fig. 4. Daily rainfall distribution, daily ET simulated by HYDRUS-1D, ASTER/S-SEBI and WDI remote sensing estimates, over Site 1 (top) and Site 4 (bottom) throughout the 2007–2008 period. Continuous lines represent HYDRUS-1D simulated ET and dotted lines represent Penman-Monteith reference evapotranspiration (ET_0). Missing ET values from WDI on 2 Nov 2007 resulted from negative WDI values because of pixels located left of the wet edge (Fig. 2). This was also observed on archive image of 8 Feb 2003, and was ascribed to errors on ground based and remote sensing data as suggested by Moran et al. (1996).

Regardless of considered ground truthing (i.e. direct estimates from EC measurements on two of the seven validation sites – Site 6 and 7 – or indirect estimates from HYDRUS-1D simulations on the seven validation sites), the validation exercise provided similar results for S-SEBI and WDI estimates of daily ET, where slightly better results were obtained with S-SEBI. When validating ASTER/S-SEBI (respectively ASTER/WDI) retrievals against EC based estimates over Site 6 and Site 7, a 0.5 $mm.d^{-1}$ RMSE value and a 0.82 determination coefficient (respectively 1.1 $mm.d^{-1}$ and 0.66) were obtained (Fig. 5a and c respectively). When validating ASTER/S-SEBI (respectively ASTER/WDI) retrievals against HYDRUS-1D based estimates over the seven validation sites (including the two sub sites 6N and 6S), a 0.8 $mm.d^{-1}$ RMSE value and a 0.74 coefficient determination (respectively 1.1 $mm.d^{-1}$ and 0.52) were obtained (Fig. 5b and d respectively). Regardless of considered ground truthing (i.e. direct estimates from EC measurements or indirect estimates from HYDRUS-1D simulations), a larger unsystematic error was observed for WDI as compared to S-SEBI, with greater discrepancies around the regression lines.

Table 4 summarized statistics for S-SEBI and WDI models on a site basis and a year basis. For S-SEBI, determination coefficients ranged from 0.52 to 0.90, and RMSE ranged from 0.5 to 1.3 $mm.d^{-1}$ (from 26% to 56% in relative). Validation results for WDI were worse, with

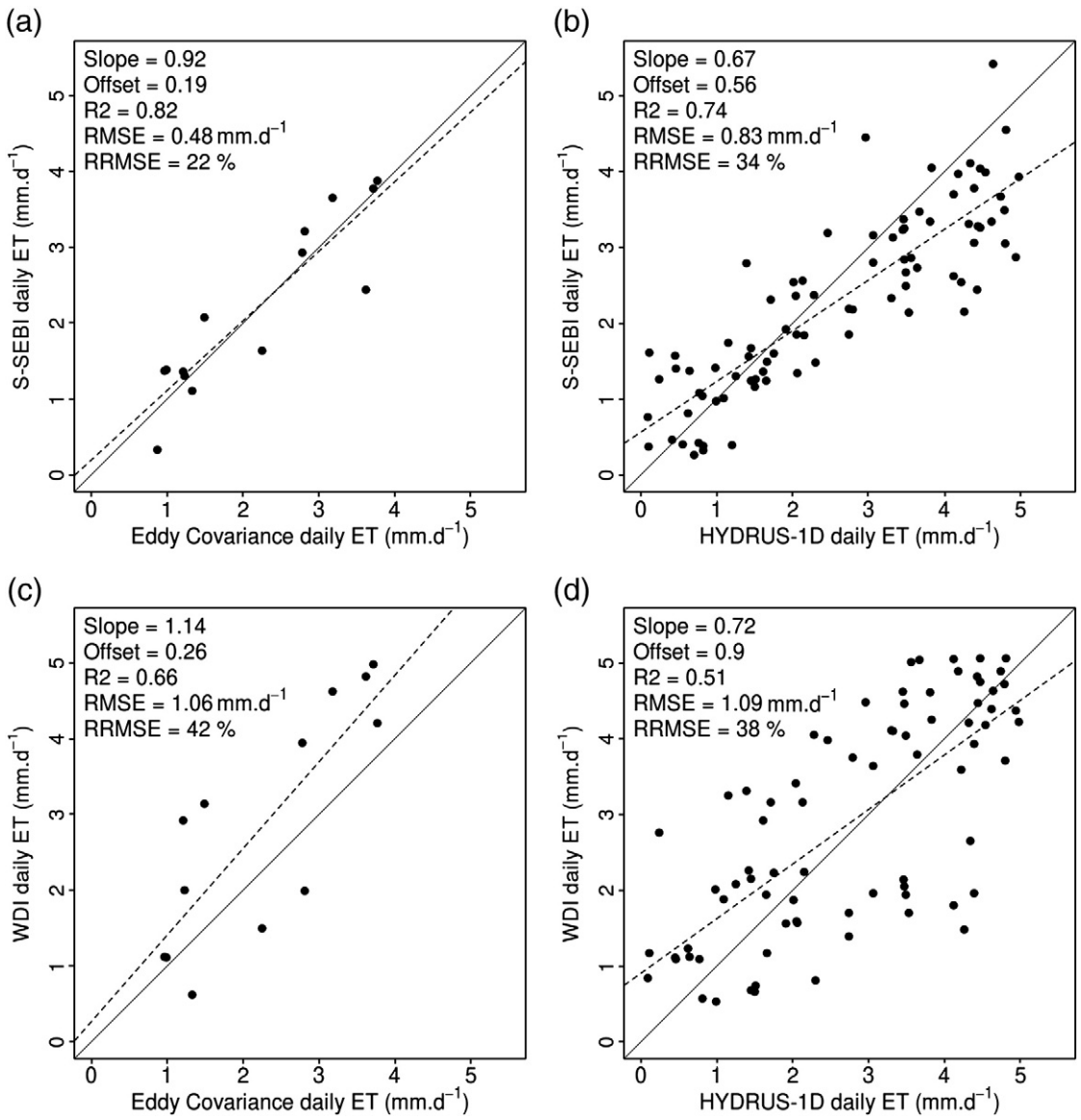

Fig. 5. Comparison of ASTER/S-SEBI (upper subplots) and ASTER/WDI (lower subplots) retrievals of daily ET against those derived from EC estimates within Site 6 and 7 (left subplots), and from HYDRUS-1D simulations over the seven validation sites (right subplots). R2 is determination coefficient. Slope and offset result from linear regression (dotted line) between x (reference estimates from EC data or HYDRUS-1D simulations) and y (ASTER remotely sensed estimates from S-SEBI or WDI) axis data. RMSE is Root Mean Square Error. RRMSE is Relative Root Mean Square Error calculated as the ratio of RMSE to reference mean value. Continuous line is the 1:1 line.

Table 4
Summary of statistics when validating ASTER/S-SEBI and ASTER/WDI estimates of daily ET against ground based estimates from HYDRUS-1D simulations: absolute and Relative Root Mean Square Error (RMSE and RRMSE), slope and offset from linear regression between ASTER estimates and HYDRUS-1D simulations, and determination coefficient R2. Results for Sites 1–7 include data from both 2007 and 2008. The last two rows indicate aggregate results for all sites partitioned by year.

		Model									
		S-SEBI					WDI				
		Slope	Offset ($mm.d^{-1}$)	R2	RMSE ($mm.d^{-1}$)	RRMSE (%)	Slope	Offset ($mm.d^{-1}$)	R2	RMSE ($mm.d^{-1}$)	RRMSE (%)
Site	1	0.54	0.9	0.76	0.1	40	0.66	0.8	0.58	1.1	37
	2	0.73	0.4	0.83	0.5	26	0.84	0.9	0.44	1.2	45
	3	0.77	0.5	0.90	0.6	28	0.65	1.3	0.60	1.2	50
	4	0.94	0.0	0.71	0.6	23	1.54	1.8	0.46	1.1	36
	5	0.62	0.4	0.86	1.0	37	0.73	0.7	0.44	1.1	34
	6N	0.65	0.6	0.77	0.7	29	0.91	0.4	0.66	0.8	31
	6S	0.80	0.8	0.86	0.7	25	0.69	0.9	0.56	1.1	38
	7	0.45	0.6	0.82	1.3	56	0.65	1.2	0.59	1.0	32
Year	2007	0.76	0.5	0.52	0.7	57	0.67	1.3	0.32	1.3	75
	2008	0.68	0.5	0.69	0.9	30	0.83	0.5	0.53	1.0	33

determination coefficients ranging from 0.32 to 0.66 and RMSE ranging from 0.8 to 1.3 mm.d^{-1} (from 31% to 75% in relative). Overall, S-SEBI performed better than WDI for the two years and for the seven sites apart from Site 7.

On a site basis, RMSE for WDI decreased from 1.2 to 0.8 mm.d^{-1} while RMSE for S-SEBI oppositely increased from 0.6 to 1.3 mm.d^{-1}. This resulted in a determination coefficient between these RMSE values of 0.25 when including all sites, and of 0.7 when removing Sub-Site 6N. A deeper analysis showed RMSE for S-SEBI (respectively WDI) decreased (respectively increased) when row orientation (Table 1) changed from −50° West to +50° East (North being 0°), with a determination coefficient around 0.5. On the other hand, no correlation was found between RMSE for S-SEBI or WDI and watertable conditions, soil color or soil type.

On a year basis, results were better for both models in 2008 (eight ASTER snapshots) than in 2007 (three ASTER snapshots). When focusing on finer timescale, both models provided dynamics similar to that simulated by HYDRUS-1D (Fig. 4), but few differences were observed. S-SEBI provided better estimates apart from 15 Jul 2008, 24 Jul 2008 and 31 Jul 2008, where it underestimated retrievals from both WDI and HYDRUS-1D. Beyond Site 1 and Site 4 used as instances for Fig. 4, underestimation from S-SEBI was observed for all validation sites on these three dates.

3.3. Comparing remote sensing retrievals at the watershed extent

Intercomparing S-SEBI and WDI estimates of daily ET at the watershed extent showed both models provided similar results, as displayed in Fig. 6 where all 20 dates of ASTER overpass were considered, either prior to (nine archive imageries between 2002 and mid 2007) or during (11 imageries between mid 2007 and late 2008) the field experiment. Corresponding statistics were a quadratic difference of 1.1 mm.d^{-1} (39% in relative), a determination coefficient of 0.52 and a 0.95 slope value when computing linear regression between both predictions. Similar results were obtained when restricting the comparison over the seven validation sites (figure not shown), with a quadratic difference of 1 mm.d^{-1} (40% in relative), a 0.61 determination coefficient and a 1.1 slope value. Therefore, both intercomparisons, either over the seven validation sites or over the whole watershed, provided similar results to those obtained with validation exercises (Section 3.2), where RMSE values ranged between 0.8 and 1.1 mm.d^{-1}, and determination coefficients ranged between 0.5 and 0.9.

Through plot density that represents occurrence frequencies, Fig. 6 also indicates the existence of three clusters. The first group is located above the regression line, and corresponds to large ET values that occur during spring and early summer. In this case, WDI retrievals significantly overestimated S-SEBI estimates of daily ET. The second group is located on the regression line and corresponds to an intermediary situation, where medium ET values occur during early spring and middle summer. In this case, WDI retrievals slightly overestimated S-SEBI estimates. The third group is located close to the 1:1 line and corresponds to low ET values that occur at the summer end. This case corresponds to the better agreement between both retrievals, with slight underestimation of S-SEBI estimates by WDI retrievals.

We finally focused on time-average values of daily ET maps by considering median values over estimates obtained during periods of maximum vegetation cover (15 Aug 2005, 10 Jul 2006, 13 Jul 2007, 14 Aug 2007, 15 Sep 2007, 8 Jul 2008, 15 Jul 2008, 24 Jul 2008, 31 Jul 2008, 1 Sep 2008, 26 Sep 2008, and 3 Oct 2008). Maps of median values derived from S-SEBI and WDI estimates are displayed in Fig. 7. It is shown that similar spatial patterns were depicted from both S-SEBI and WDI estimates, where (i) the corresponding coefficients of

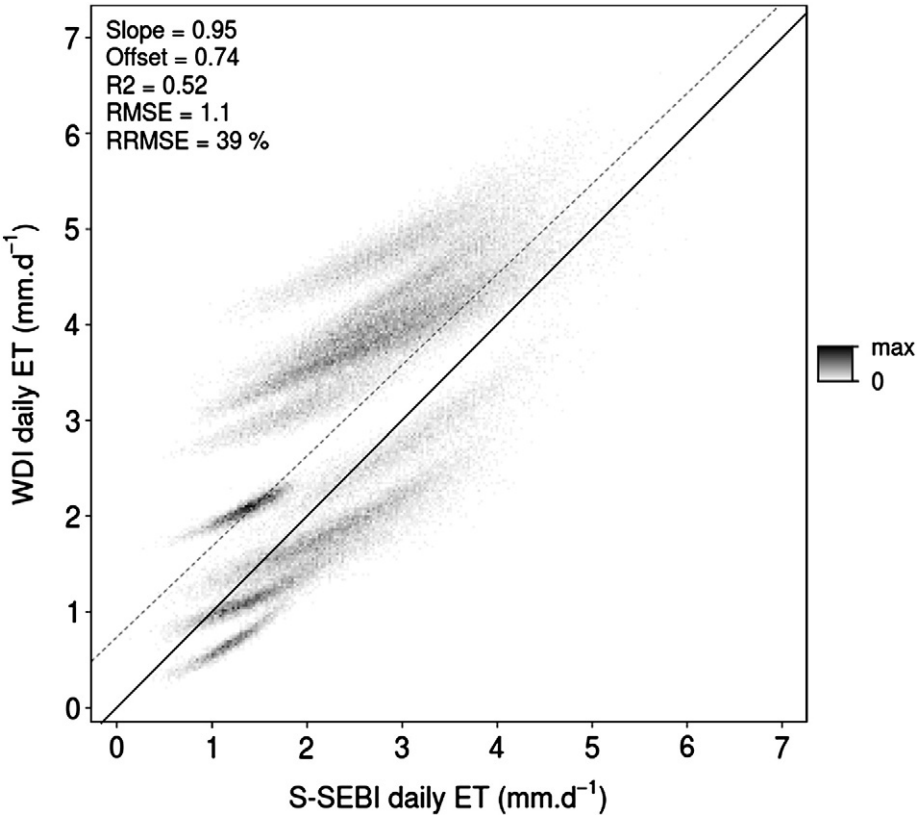

Fig. 6. Intercomparison, at the extent of the Peyne watershed, between daily ET estimates derived from ASTER imagery through S-SEBI and WDI. Dashed line is the 1:1 line. R2 is determination coefficient, Slope and Offset results from linear regression (dotted line) between x (S-SEBI estimates) and y (WDI estimates) axis data. Continuous line is the 1:1 line. Gray scale represents occurrence frequencies.

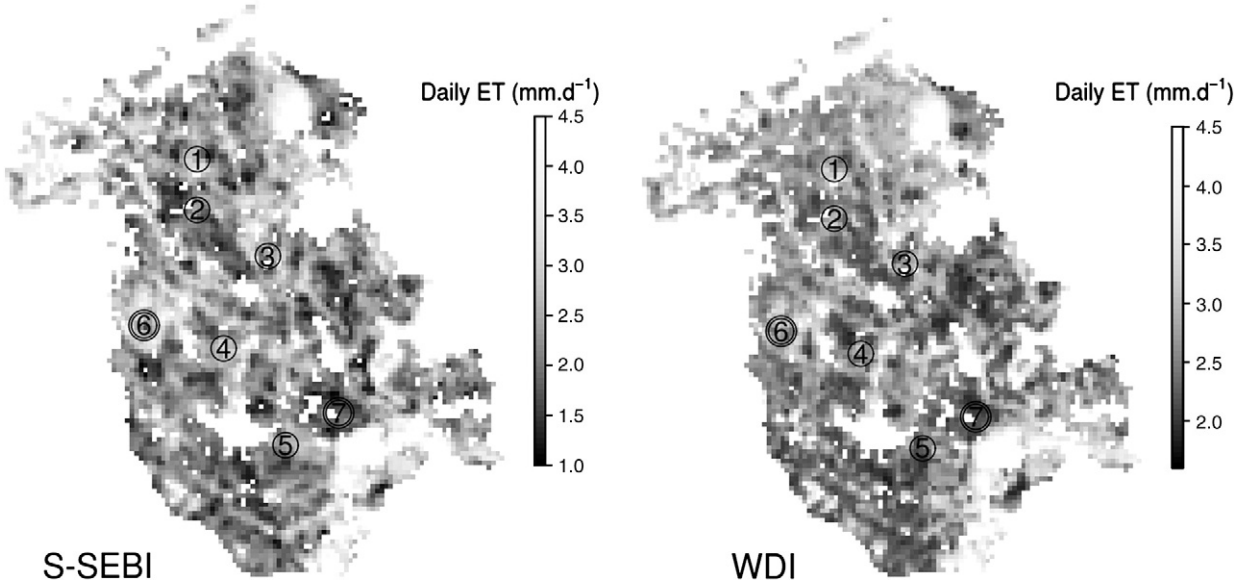

Fig. 7. Maps of time-averaged (median values) daily ET from S-SEBI (left) and WDI (right), where median values were computed over estimates obtained during the period of maximum vegetation cover. Validation sites are labeled 1 to 7, and double circles correspond to sites with EC measurements (Site 6 and Site 7). Missing values are white.

variation ranged between 0 and 40%, and (ii) differences between S-SEBI and WDI estimates were within 1 mm.d^{-1}. Median ET values ranged between 1 and 4.5 mm.d^{-1} and depict a Gaussian distribution in magnitude. Patterns of low and large values were disseminated within the watershed.

4. Discussion

When comparing HYDRUS-1D simulations of soil moisture profiles against NP measurements, the lowering of RMSE with depth was ascribed to a larger temporal stability for water flows within deep soil layers, whereas the largest RMSE values around 1 m depth were imputed to temporal variations of soil moisture in relation to root water uptake. Further, the diminution of RMSE with simulation time was explained by stabilization of numerical computations as simulation time increased, in relation to possible errors in HYDRUS-1D initialization. Finally, the obtaining of a 10% relative accuracy on simulated soil water storage at noon was considered as acceptable, given (i) the large suite of conditions in soil type and watertable level, and (ii) the uncertainties on NP data, about 15% in relative (Section 2.2.1).

When comparing HYDRUS-1D estimates of daily ET against EC based retrievals, the larger differences observed for Site 6 were ascribed to a larger amount of data (continuous measurements over nine locations of NP measurements versus temporary measurements over one location for Site 7). Differences between HYDRUS-1D simulations and EC estimates after large or lengthy rainfalls could be explained by HYDRUS-1D deficiencies, such as an inadequate characterization of vegetation functioning and/or the lack of consideration for both inter-row weeding and lateral water flows within the vadoze zone. The slightly lower RMSE value we obtained when restricting the dataset to ASTER overpass days (0.5 mm.d^{-1}) was ascribed to meteorological conditions that were favorable under clear sky conditions. Overall, the obtained accuracy, around 0.6 mm.d^{-1}, was close to that required for further applications, of about 0.8 mm.d^{-1} (Kalma et al., 2008; Seguin et al., 1999). As compared to outcomes reported in the literature for lower spatial extents and summer periods only (Bsaibes, 2007; Trambouze et al., 1998), the current study enlarged the assessment of HYDRUS-1D capabilities, with similar RMSE values ranging from 0.4 to 0.6 mm.d^{-1}. Finally, these results were obtained by comparing two independent estimation methods, based either on near surface turbulent fluxes (EC measurements) or on vadose-zone water transfers (HYDRUS-1D simulations). This emphasized the pertinence of HYDRUS-1D simulations for being used as ground truthing of daily ET estimates.

Despite the satisfactory simulations of daily ET obtained with the HYDRUS-1D model, implementing the latter over the seven validation sites was not straightforward. Indeed, this implementation required a large number of inputs in relation to pedological conditions, water-table level, soil moisture profile, root distribution, canopy structure and reference evapotranspiration. Such field information is usually difficult to collect, especially when dealing with hydrodynamic properties (e.g. soil horizons and related textures, profiles of root density). To avoid these difficulties, we concentrated the experimental efforts on the most important HYDRUS-1D inputs that were previously identified by Bsaibes (2007) through a sensitivity analysis conducted under similar environmental conditions. This study showed HYDRUS-1D simulations were more sensitive to canopy height, trellis width and watertable level (relative variations from the reference simulation of about 25%) than to root profile, horizon distribution and topsoil characteristics (relative variations from the reference simulation lower than 10%). Thereby, we obtained good simulations with the physical HYDRUS-1D model once it was well documented for the key inputs that drive model simulations.

The specific periods we observed when analyzing the temporal dynamics of HYDRUS-1D simulations suggested foreseeing a larger panel of possible factors that drive vineyard ET. Indeed larger values of daily ET where observed during the [May–July] period over a validation site with supposedly restrictive water conditions (Site 1), as compared to another validation site with permanent watertable (Site 4). Additional factors to be suspected were (i) agricultural practices such as inter-row weeding and canopy thinning, (ii) water balance after large and lengthy rainfall that may induce waterlogging, and (iii) plant physiology in relation to adaptation to pedo-climatic conditions since the grape variety established within Site 1 (Syrah) was premature as compared to that established on Site 4 (Cabernet Sauvignon).

The 45 W.m^{-2} RMSE value obtained when validating ASTER retrievals of net radiation against ground based measurements was larger than those usually reported in the literature (French et al., 2005; Gomez et al., 2005; Jacob et al., 2002; Timmermans et al., 2007). This was ascribed to the difference between the vegetation cover fraction within the Campbell NR-lite footprint and that within the

ASTER pixel (66% versus 40% for maximum vegetation cover fraction, Section 2.2.1). Further, the 0.4 mm.d^{-1} value obtained for daily ET standard deviation within 3×3 pixel windows centered on validation sites was lower than accuracy on ground based estimates (around 0.6 mm.d^{-1}). This indicated the spatial variability at the ASTER spatial resolution in the neighborhood of validation sites had no significant influence on the validation exercise.

Validation exercises for ASTER/S-SEBI and ASTER/WDI over the seven validation sites indicated performances similar to those reported in the literature for S-SEBI (no validation exercise was found for WDI retrievals of daily ET), where these performances range between 1 and 1.5 mm.d^{-1} for finer (~20 m) and coarser (~1 km) spatial resolutions (Boronina & Ramillien, 2008; Gomez et al., 2005; Roerink et al., 2000; Sobrino, Gomez, et al., 2007; Sobrino et al., 2005; Verstraeten et al., 2005). On the one hand, S-SEBI performances were better than WDI ones by 25% in relative, along with lower unsystematic errors. On the other hand, WDI deterministically calculates evaporative extremes through the inversion of sensible heat flux along with meteorological data, whereas S-SEBI determines these extremes from variabilities captured within thermal infrared imagery–concept of contextual model as proposed by Kalma et al. (2008). Then, poor performances for WDI may be related to the inclusion of significant errors into flux calculations, since meteorological forcing at the watershed extent was characterized from a unique measurement location within Site 6. Overall, the obtaining of better performances with the contextual model was in agreement with conclusions from Timmermans et al. (2007) and Kalma et al. (2008) who reported physically based models are not necessarily more accurate. This raises the question of compromising between process description and measurement availability, where further investigations will focus on sensitivity analysis for both WDI and S-SEBI models in relation to their underlying assumptions.

Validation results on a site basis showed correlations between model performances, in relation to row orientation, which suggested the latter drove the accuracy of remotely sensed retrievals. The influence could be radiative, with illumination and shadow effects on ASTER data according to sun position and row orientation, as already pointed out by Zarco-Tejada et al. (2005). The influence could also be aerodynamic, with the coupling between wind direction and row orientation that affects vineyard ET (Heilman et al., 1996). This aerodynamic issue might be sharpened by strong wind speeds that are usual within the Peyne watershed. Therefore, future investigations should address the inclusion of row orientation, where the latter can be retrieved from aerial images with automatized frequency analysis (Delenne et al., 2008).

From a temporal viewpoint, we noted S-SEBI performed worse than WDI for specific dates during early summer. A possible explanation is the failure of the assumption on which rely contextual models (and therefore S-SEBI), where it is assumed the variability captured within the thermal infrared imagery is large enough for properly characterizing water status over the whole study area. In our case, this failure may be ascribed to a lack of dry conditions within the watershed, because of water storage filling after spring rainfalls. This was in agreement with conclusions from Vidal and Devaux-Ros (1995) who addressed the performances of the triangle method (a contextual model) when used along with Landsat data on early summer.

Intercomparison of ASTER/S-SEBI and ASTER/WDI retrievals at the watershed extent provided results similar to those obtained when intercomparing over the validation sites or when validating against ground based estimates. This *a posteriori* confirmed the choice of the validation sites for capturing the variability within the watershed that included a larger range of environmental conditions. Overall, obtained differences between models are within the range of accuracies reported in the literature, between 1 and 1.5 mm.d^{-1} (Boronina & Ramillien, 2008; Gomez et al., 2005; Roerink et al., 2000; Sobrino, Gomez, et al., 2007; Sobrino et al., 2005; Verstraeten et al., 2005), and close to the 0.8 mm.d^{-1} accuracy regularly quoted in literature as a requirement for many applications (Kalma et al., 2008; Seguin et al., 1999). On the other hand, intercomparison at the watershed extent emphasized three groups of scatterplots that correspond to different periods of the year, and therefore to different magnitudes in terms of ET and vegetation cover fraction. Further investigations are necessary for deepening these differences, which may result either from the ways the models characterized the evaporative extremes or from the characterization of spatial variability through albedo or vegetation cover fraction (Merlin et al., 2010).

Finally, averaging maps of daily ET over the period of maximum vegetation cover underlined the existence of spatial patterns at the watershed extent. Given that we focus on perennial plants with deep rooting systems, these spatial structures may result from pedological and landscape conditions such as soil depth and texture, watertable level, solar exposure, and position within the watershed. Ongoing investigations address a possible link between these factors and the observed spatial patterns.

5. Conclusion

The objective of this study was to compare the performances of two differencing methods for the retrieval of daily ET over a Mediterranean vineyard watershed. The S-SEBI and WDI models were implemented with ASTER imagery, and validated during almost two growth cycles in 2007 and 2008. Validation against HYDRUS-1D simulations was conducted over seven contrasted sites that depicted important dynamics of daily ET in relation to soil and watertable conditions. S-SEBI and WDI were also intercompared at the watershed extent by considering ASTER imagery collected over the 2002–2008 period.

Within two of the seven validation sites, HYDRUS-1D simulations were controlled through a comparison against reference estimates based on EC measurements. Thus, the differences between HYDRUS-1D simulations and EC estimates were about 0.6 mm.d^{-1}. Validation of S-SEBI and WDI estimates against HYDRUS-1D simulations indicated accuracies between 0.8 mm.d^{-1} and 1.1 mm.d^{-1}. These accuracies were close to that regularly quoted in the literature as a requirement for further applications (Kalma et al., 2008; Seguin et al., 1999). The simpler approach (S-SEBI) produced better results than the more physical method (WDI), which raised the question of compromising between process description and measurement availability. A deeper analysis of these validation results suggested a partial influence of row orientation for both models. Model intercomparison over the seven validation sites only and at the watershed extent provided results close to those obtained from validation, with quadratic differences around 1 mm.d^{-1}. Finally, multi-date inspection suggested the existence of spatial patterns at the watershed extent, which was ascribed to landscape conditions in relation to soil depth, soil type and watertable level.

Future works will address (i) model sensitivities to their underlying assumptions, in relation to the compromising between process description and measurement availability, (ii) inclusion within model parameterizations of row orientation that can be characterized from remote sensing data collected at very high spatial resolution, and (iii) the possible links between the spatial structures we observed on daily ET maps and the landscape conditions.

Acknowledgments

The authors thank the LISAH technical staff for the experiment, and the Jet Propulsion Laboratory for ASTER data collection. This study was funded by the Chilean National Commission for Scientific and Technological Research, by the French National Institute for Agricultural Research and the French National Program for Remote Sensing.

References

Abrams, M. (2000). The Advanced Spaceborne Thermal Emission and Reflection radiometer (ASTER): Data products for the high spatial resolution imager on NASA's Terra platform. *International Journal of Remote Sensing*, *21*, 847—859.

Bastiaanssen, W. G. M., Menenti, M., Feddes, R. A., & Holtslag, A. A. M. (1998). A remote sensing surface energy balance algorithm for land (SEBAL). 1. Formulation. *Journal of Hydrology*, *212–213*, 198—212.

Boegh, E., Poulsen, R., Butts, M., Abrahamsen, P., Dellwik, E., Hansen, S., et al. (2009). Remote sensing based evapotranspiration and runoff modeling of agricultural, forest and urban flux sites in Denmark: From field to macro-scale. *Journal of Hydrology*, *377*(3–4), 300—316.

Boronina, A., & Ramillien, G. (2008). Application of AVHRR imagery and GRACE measurements for calculation of actual evapotranspiration over the Quaternary aquifer (Lake Chad basin) and validation of groundwater models. *Journal of Hydrology*, *348*(1–2), 98—109.

Brutsaert, W. (1975). On a derivable formula for long-wave radiation from clear skies. *Water Resources Research*, *11*(5), 742—744.

Bsaibes, A., 2007. Évaluation d'une approche multi-locale d'estimation spatiale de l'évapotranspiration. Ph.D. thesis, Université de Montpellier II.

Chehbouni, A., Hoedjes, J. C., Rodriquez, J. -C., Watts, C. J., Garatuza, J., Jacob, F., et al. (2008). Using remotely sensed data to estimate area-averaged daily surface fluxes over a semi-arid mixed agricultural land. *Agricultural and Forest Meteorology*, *148*(3), 330—342.

Choi, M., Kustas, W. P., Anderson, M. C., Allen, R. G., Li, F., & Kjaersgaard, J. H. (2009). An intercomparison of three remote sensing-based surface energy balance algorithms over a corn and soybean production region (Iowa, U.S.) during SMACEX. *Agricultural and Forest Meteorology*, *149*(12), 2082—2097.

Clothier, B. (1986). Estimation of soil heat flux from a net radiation during the growth of alfalfa. *Agricultural and Forest Meteorology*, *37*, 319—329.

Courault, D., Jacob, F., Benoit, V., Weiss, M., Marloie, O., Hanocq, J. -F., et al. (2009). Influence of agricultural practices on micrometeorological spatial variations at local and regional scales. *International Journal of Remote Sensing*, *30*(5), 1183—1205.

Courault, D., Lacarrère, P., Clastre, P., Lecharpentier, P., Jacob, F., Marloie, O., et al. (2003). Estimation of surface fluxes in a small agricultural area using the three-dimensional atmospheric model Meso-NH and remote sensing data. *Canadian Journal of Remote Sensing*, *29*, 741—754.

Courault, D., Seguin, B., & Olioso, A. (2005). Review on estimation of evapotranspiration from remote sensing data: From empirical to numerical modeling approaches. *Irrigation and Drainage Systems*, *19*(3), 223—249.

Daneshkar Arasteh, P., & Tajrishy, M. (2008). Calibrating Priestley-Taylor model to estimate open water evaporation under regional advection using volume balance method-case study: Chahnimeh reservoir, Iran. *Journal of Applied Science*, *8*(22), 4097—4104.

de Wit, C., Goudriaan, J., van Laar, H., Penning de Vries, F., Rabbinge, R., van Keulen, H., et al. (1978). *Simulation of assimilation, respiration and transpiration of crops*. Simulation monographs. Wageningen, The Netherlands: Centre for Agricultural Publishing and Documentation (PUDOC) 141 pp., ISBN 90-220-0601-8.

Delenne, C., Rabatel, G., & Deshayes, M. (2008). An automatized frequency analysis for vine plot detection and delineation in remote sensing. *IEEE Geoscience and Remote Sensing Letters*, *5*(3), 341—345.

Diffenbaugh, N., Pal, J., Giorgi, F., & Gao, X. (2007). Heat stress intensification in the Mediterranean climate change hotspot. *Geophysical Research Letters*, *34*(11), L11706.

Dijk, A. V., Moene, A., & Bruin, H. D. (2004). The principle of surface flux physics: Theory, practice and description of the ECPACK library, internal report 2004/1. Tech. rep. Wageningen, The Netherlands: Meteorology and Air Quality Group, Wageningen University.

Er-Raki, S., Chehbouni, A., Guemouria, N., Duchemin, B., Ezzahar, J., & Hadria, R. (2007). Combining FAO-56 model and ground-based remote sensing to estimate water consumptions of wheat crops in a semi-arid region. *Agricultural Water Management*, *87*(1), 41—54.

Feddes, R., Kowalik, P., & Zaradny, H. (1978). *Simulation of field water use and crop yield*. Simulation monographs. Wageningen, The Netherlands: PUDOC.

Flexas, J., Briantais, J. -M., Cerovic, Z., Medrano, H., & Moya, I. (2000). Steady-state and maximum chlorophyll fluorescence responses to water stress in grapevine leaves: a new remote sensing system. *Remote Sensing of Environment*, *73*(3), 283—297.

French, A., Jacob, F., Anderson, M., Kustas, W., Timmermans, W., Gieske, A., et al. (2005). Surface energy fluxes with the Advanced Spaceborne Thermal Emission and Reflection radiometer (ASTER) at the Iowa 2002 SMACEX site (USA). *Remote Sensing of Environment*, *99*(1–2), 55—65.

French, A., Schmugge, T., Ritchie, J., Hsu, A., Jacob, F., & Ogawa, K. (2008). Detecting land cover change at the Jornada Experimental Range, New Mexico with ASTER emissivities. *Remote Sensing of Environment*, *112*(4), 1730—1748.

Galleguillos, M., Jacob, F., Prévot, L., Lagacherie, P., & Liang, S. (2011). Mapping daily evapotranspiration over a Mediterranean vineyard watershed. *IEEE Geosciences and Remote Sensing Letters*, *8*(1), 168—172.

Gillies, R. R., Carlson, T. N., Kustas, W. P., & Humes, K. S. (1997). A verification of the 'triangle' method for obtaining surface soil water content and energy fluxes from remote measurements of the normalized difference vegetation index (NDVI) and surface radiant temperature. *International Journal of Remote Sensing*, *18*(15), 3145—3166.

Giordani, H., Noilhan, J., Lacarrère, P., Bessemoulin, P., & Mascart, P. (1996). Modelling the surface processes and the atmospheric boundary layer for semi-arid conditions. *Agricultural and Forest Meteorology*, *80*(2–4), 263—287.

Giorgi, F. (2006). Climate change hot-spots. *Geophysical Research Letters*, *33*(8), L08707.

Gomez, M., Olioso, A., Sobrino, J., & Jacob, F. (2005). Retrieval of evapotranspiration over the Alpilles/ReSeDA experimental site using airborne POLDER sensor and a thermal camera. *Remote Sensing of Environment*, *96*, 399—408.

Heilman, J., McInnes, K., Gesch, R., Lascano, R., & Savage, M. (1996). Effects of trellising on the energy balance of a vineyard. *Agricultural and Forest Meteorology*, *81*, 79—93.

Heilman, J., McInnes, K., Savage, M., Gesch, R., & Lascano, R. (1994). Soil and canopy energy balances in a west Texas vineyard. *Agricultural and Forest Meteorology*, *71*(1–2), 99—114.

Hoedjes, J., Chehbouni, A., Jacob, F., Ezzahar, J., & Boulet, G. (2008). Deriving daily evapotranspiration from remotely sensed instantaneous evaporative fraction over olive orchard in semi-arid Morocco. *Journal of Hydrology*, *354*(1–4), 53—64.

Holifield, C., McElroy, S., Moran, M., Bryant, R., Miura, T., & Emmerich, W. E. (2003). Temporal and spatial changes in grassland transpiration detected using Landsat TM and ETM + imagery. *Canadian Journal of Remote Sensing*, *29*(2), 259—270.

Huete, A. (1988). A soil-adjusted vegetation index (SAVI). *Remote Sensing of Environment*, *25*(3), 295—309.

Huete, A., Hua, G., Qi, J., Chehbouni, A., & van Leeuwen, W. (1992). Normalization of multidirectional red and NIR reflectances with the SAVI. *Remote Sensing of Environment*, *41*(2–3), 143—154.

Jackson, R., Hatfield, J., Reginato, R., Idso, S., & Pinter, P. J. (1983). Estimation of daily evapotranspiration from one time-of-day measurements. *Agricultural Water Management*, *7*(1–3), 351—362.

Jacob, F., Olioso, A., Gu, X. F., Su, Z., & Seguin, B. (2002). Mapping surface fluxes using airborne visible near infrared, thermal infrared remote sensing data and a spatialized surface energy balance model. *Agronomie*, *22*, 669—680.

Jacob, F., Petitcolin, F., Schmugge, T., Vermote, É., French, A., & Ogawa, K. (2004). Comparison of land surface emissivity and radiometric temperature derived from MODIS and ASTER sensors. *Remote Sensing of Environment*, *90*(2), 137—152.

Jacob, F., Schmugge, T., Olioso, A., French, A., Courault, D., Ogawa, K., et al. (2008). Modeling and inversion in thermal infrared remote sensing over vegetated land surfaces. In S. Liang (Ed.), *Advances in land remote sensing: System, modeling, inversion and application*, Springer 2008 XXII (ISBN 978-1-4020-6449-4), p. 245–292.

Kalma, J. D., McVicar, T. R., & McCabe, M. F. (2008). Estimating land surface evaporation: a review of methods using remotely sensed surface temperature data. *Surveys in Geophysics*, *29*(4–5), 421—469.

Lebon, E., Dumas, V., Pieri, P., & Schultz, H. R. (2003). Modelling the seasonal dynamics of the soil water balance of vineyards. *Functional Plant Biology*, *30*, 699—710.

Li, S., Kang, S., Li, F., Zhang, L., & Zhang, B. (2008). Vineyard evaporative fraction based on eddy covariance in an arid desert region of Northwest China. *Agricultural Water Management*, *95*(8), 937—948.

Li, F., & Lyons, T. (1999). Estimation of regional evapotranspiration through remote sensing. *Journal of Applied Meteorology*, *38*, 1644—1654.

Li, S., Tong, L., Li, F., Zhang, L., Zhang, B., & Kang, S. (2009). Variability in energy partitioning and resistance parameters for a vineyard in northwest China. *Agricultural Water Management*, *96*(6), 955—962.

Liang, S. (2001). Narrowband to broadband conversions of land surface albedo I: Algorithms. *Remote Sensing of Environment*, *76*(2), 213—238.

Luquet, D., Bégué, A., Vidal, A., Clouvel, P., Dauzat, J., Olioso, A., et al. (2003). Using multidirectional thermography to characterize water status of cotton. *Remote Sensing of Environment*, *84*(3), 411—421.

Mendez-Barroso, L. A., Garatuza-Payan, J., & Vivoni, E. R. (2008). Quantifying water stress on wheat using remote sensing in the Yaqui valley, Sonora, Mexico. *Agricultural Water Management*, *95*(6), 725—736.

Menenti, M., & Choudhury, B. (1993). Parameterization of land surface evapotranspiration using a location-dependent potential evapotranspiration and surface temperature range. In H. Bolle (Ed.), *Exchange processes at the land surface for a range of space and time scales* (pp. 561—568). : IAHS.

Merlin, O., Duchemin, B., Hagolle, O., Jacob, F., Coudert, B., Chehbouni, G., Dedieu, G., Garatuza, J., & Kerr, Y. (2010). Disaggregation of MODIS Surface Temperature over an Agricultural Area Using Time Series of Formosat-2 Images. *Remote Sensing of Environment*, *114*(11), 2500—2512.

Montero, F., Meliab, J., Brasa, A., Segarra, D., Cuesta, A., & Lanjeri, S. (1999). Assessment of vine development according to available water resources by using remote sensing in La Mancha, Spain. *Agricultural Water Management*, *40*, 363—375.

Moran, M., Clarke, T., Inoue, Y., & Vidal, A. (1994). Estimating crop water deficit using the relation between surface–air temperature and spectral vegetation index. *Remote Sensing of Environment*, *49*(3), 246—263.

Moran, M., Rahman, A., Washburne, J., Goodrich, D., Weltz, M., & Kustas, W. (1996). Combining the Penman-Monteith equation with measurements of surface temperature and reflectance to estimate evaporation rates of semiarid grassland. *Agricultural and Forest Meteorology*, *80*(2–4), 87—109.

Moussa, R., Chahinian, N., & Bocquillon, C. (2007). Distributed hydrological modelling of a Mediterranean mountainous catchment — Model construction and multi-site validation. *Journal of Hydrology*, *337*(1–2), 35—51.

Moya, I., Camenen, L., Evain, S., Goulas, Y., Cerovic, Z. G., Latouche, G., et al. (2004). A new instrument for passive remote sensing: 1. Measurements of sunlight-induced chlorophyll fluorescence. *Remote Sensing of Environment*, *91*(2), 186—197.

Neuman, S., Feddes, R., & Bresler, E. (1974). *Finite element simulation of flow in saturated-unsaturated soils considering water uptake by plants*. Tech. rep., Third Annual Report, Project No. A10-SWC-77.

Norman, J. M., Kustas, W. P., & Humes, K. S. (1995). Source approach for estimating soil and vegetation energy fluxes in observations of directional radiometric surface temperature. *Agricultural and Forest Meteorology*, *77*(3–4), 263—293.

Ogawa, K., Schmugge, T., Jacob, F., & French, A. (2003). Estimation of land surface window (8–12 μm) emissivity from multi-spectral thermal infrared remote sensing — a case study in a part of Sahara desert. *Geophysical Research Letters*, *30*(2), 1067.

Olioso, A., Inoué, Y., Ortega-Farias, S., Demarty, J., Wigneron, J., Braud, I., et al. (2005). Future directions for advanced evapotranspiration modeling: Assimilation of remote sensing data into crop simulation models and svat models. *Irrigation and Drainage Systems*, *19*, 377—412.

Oliver, H., & Sene, K. (1992). Energy and water balances of developing vines. *Agricultural and Forest Meteorology*, *61*(3–4), 167—185.

Ortega-Farias, S., Carrasco, M., Olioso, A., Acevedo, C., & Poblete, C. (2007). Latent heat flux over Cabernet Sauvignon vineyard using the Shuttleworth and Wallace model. *Irrigation Science*, *25*(2), 161—170.

Pellegrino, A., Goze, E., Lebon, E., & Wery, J. (2006). A model-based diagnosis tool to evaluate the water stress experienced by grapevine in field sites. *European Journal of Agronomy*, *25*(1), 49—59.

Richards, L. (1931). Capillary conduction of liquids through porous media. *Physics*, *1*, 318—333.

Riou, C., Pieri, P., & Clech, B. L. (1994). Consommation d'eau de la vigne en conditions hydriques non limitantes. Formulation simplifiée de la transpiration. *Vitis*, *33*, 109—115.

Roerink, G. J., Su, Z., & Menenti, M. (2000). S-SEBI: a simple remote sensing algorithm to estimate the surface energy balance. *Physics and Chemistry of the Earth. Part B: Hydrology, Oceans and Atmosphere*, *25*(2), 147—157.

Sabol, D. E., Gillespie, A. R., Abbott, E., & Yamada, G. (2009). Field validation of the ASTER temperature-emissivity separation algorithm. *Remote Sensing of Environment*, *113*(11), 2328—2344.

Sanchez, J., Kustas, W., Caselles, V., & Anderson, M. (2008). Modelling surface energy fluxes over maize using a two-source patch model and radiometric soil and canopy temperature observations. *Remote Sensing of Environment*, *112*, 1130—1143.

Seguin, B., Becker, F., Phulpin, T., Guyot, G., & Kerr, Y. (1999). IRSUTE: a minisatellite project for land surface heat flux estimation from field to regional scale. *Remote Sensing of Environment*, *68*, 357—369.

Sene, K. (1994). Parameterisations for energy transfers from a sparse vine crop. *Agricultural and Forest Meteorology*, *71*(1–2), 1—18.

Simunek, J., Sejna, M., van Genuchten, M., & Sejna, M. (2008). *The HYDRUS-1D software package for simulating the one-dimensional movement of water, heat, and multiple solutes in variably-saturated media.* Version 4.0. Dep. of Environmental Sciences. Riverside: University of California.

Sobrino, J., Gomez, M., Jimenez-Munoz, J., & Olioso, A. (2007). Application of a simple algorithm to estimate daily evapotranspiration from NOAA-AVHRR images for the Iberian Peninsula. *Remote Sensing of Environment*, *110*(2), 139—148.

Sobrino, J., Gomez, M., Jimenez-Munoz, J., Olioso, A., & Chehbouni, G. (2005). A simple algorithm to estimate evapotranspiration from DAIS data: Application to the DAISEX campaigns. *Journal of Hydrology*, *315*(1–4), 117—125.

Sobrino, J. A., Jimenez-Munoz, J. C., Balick, L., Gillespie, A. R., Sabol, D. A., & Gustafson, W. T. (2007). Accuracy of ASTER level-2 thermal-infrared standard products of an agricultural area in Spain. *Remote Sensing of Environment*, *106*(2), 146—153.

Sobrino, J. A., Jimenez-Munoz, J. C., Soria, G., Gomez, M., Ortiz, A. B., Romaguera, M., et al. (2008). Thermal remote sensing in the framework of the SEN2FLEX project: Field measurements, airborne data and applications. *International Journal of Remote Sensing*, *29*(17–18), 4961—4991.

Spano, D., Snyder, R. L., Duce, P., & Paw, U. K. T. (2000). Estimating sensible and latent heat flux densities from grapevine canopies using surface renewal. *Agricultural and Forest Meteorology*, *104*(3), 171—183.

Thom, A. S. (1975). Momentum, mass and heat exchange of plant communities. In J. L. Monteith (Ed.), *Vegetation and the atmosphere* (pp. 57—109). London: Academic press.

Thome, K., Arai, K., Hook, S., Kieffer, H., Lang, H., Matsunaga, T., et al. (1998). ASTER preflight and inflight calibration and the validation of Level 2 products. *IEEE Transactions on Geoscience and Remote Sensing*, *36*, 1161—1172.

Timmermans, W. J., Kustas, W. P., Anderson, M. C., & French, A. N. (2007). An intercomparison of the Surface Energy Balance Algorithm for Land (SEBAL) and the Two-Source Energy Balance (TSEB) modeling schemes. *Remote Sensing of Environment*, *108*(4), 369—384.

Trambouze, W., 1996. Caractérisation et éléments de modélisation de l'évapotranspiration réelle de la vigne à l'échelle de la parcelle. Ph.D. thesis, ENSAM, INRA, 191 pp.

Trambouze, W., Bertuzzi, P., & Voltz, M. (1998). Comparison of methods for estimating actual evapotranspiration in a row-cropped vineyard. *Agricultural and Forest Meteorology*, *91*(3–4), 193—208.

Trambouze, W., & Voltz, M. (2001). Measurement and modelling of the transpiration of a Mediterranean vineyard. *Agricultural and Forest Meteorology*, *107*(2), 153—166.

Valiantzas, J. D. (2006). Simplified versions for the penman evaporation equation using routine weather data. *Journal of Hydrology*, *331*(3–4), 690—702.

van der Kwast, J., Timmermans, W., Gieske, A., Su, Z., Olioso, A., Jia, L., et al. (2009). Evaluation of the Surface Energy Balance System (SEBS) applied to ASTER imagery with flux-measurements at the SPARC 2004 site (Barrax, Spain). *Hydrology and Earth System Sciences*, *13*(7), 1337—1347.

van der Tol, C., Verhoef, W., Timmermans, J., Verhoef, A., & Su, Z. (2009). An integrated model of soil-canopy spectral radiances, photosynthesis, fluorescence, temperature and energy balance. *Biogeosciences*, *6*(12), 3109—3129.

van Genuchten, M. (1980). A closed-form equation for predicting the hydraulic conductivity of unsaturated soils. *Soil Science Society of America Journal*, *44*, 892—898.

Verhoef, A., De Bruin, H. A. R., & van den Hurk, B. J. J. M. (1996). Some practical notes on the parameter kB^{-1} for sparse vegetation. *Journal of Applied Meteorology*, *36*, 560—572.

Verhoef, W., Jia, L., Xiao, Q., & Su, Z. (2007). Unified optical–thermal four-stream radiative transfer theory for homogeneous vegetation canopies. *IEEE Transactions on Geoscience and Remote Sensing*, *45*(6), 1808—1822.

Verstraeten, W. W., Veroustraete, F., & Feyen, J. (2005). Estimating evapotranspiration of European forests from NOAA-imagery at satellite overpass time: Towards an operational processing chain for integrated optical and thermal sensor data products. *Remote Sensing of Environment*, *96*(2), 256—276.

Vidal, A., & Devaux-Ros, C. (1995). Evaluating forest fire hazard with a LandSat TM derived water stress index. *Agricultural and Forest Meteorology*, *77*(3–4), 207—224.

Wang, Q., & Takahashi, H. (1999). A land surface water deficit model for an arid and semiarid region: Impact of desertification on the water deficit status in the Loess Plateau, China. *Journal of Climate*, *12*, 244—257.

Wassenaar, T., Baret, F., Robbez-Masson, J., & Andrieux, P. (2001). Sunlit soil surface extraction from remotely sensed imagery of perennial, discontinuous crop areas; the case of Mediterranean vineyards. *Agronomie: Agriculture and Environment*, *21*(3), 235—245.

Weiss, M., Baret, F., Leroy, M., Bégué, A., Hautecoeur, O., & Santer, R. (1999). Hemispherical reflectance and albedo estimates from the accumulation of across-track sun-synchronous satellite data. *Journal of Geophysical Research, [Atmospheres]*, *104*, 221—232.

Williams, L., & Ayars, J. (2005). Grapevine water use and the crop coefficient are linear functions of the shaded area measured beneath the canopy. *Agricultural and Forest Meteorology*, *132*(3–4), 201—211.

Zarco-Tejada, P., Berjon, A., Lopez-Lozano, R., Miller, J., Martin, P., Cachorro, V., et al. (2005). Assessing vineyard condition with hyperspectral indices: Leaf and canopy reflectance simulation in a row-structured discontinuous canopy. *Remote Sensing of Environment*, *99*(3), 271—287.

Zwart, S. J., & Bastiaanssen, W. G. (2007). SEBAL for detecting spatial variation of water productivity and scope for improvement in eight irrigated wheat systems. *Agricultural Water Management*, *89*(3), 287—296.